A&A 649, A103 (2021)
https://doi.org/10.1051/0004-6361/202039747

Astronomy & Astrophysics

Comparative high-resolution spectroscopy of M dwarfs: Exploring non-LTE effects

T. Olander, U. Heiter, and O. Kochukhov

Observational Astrophysics, Department of Physics and Astronomy, Uppsala University, Box 516, 75120 Uppsala, Sweden
e-mail: terese.olander@physics.uu.se; ulrike.heiter@physics.uu.se; oleg.kochukhov@physics.uu.se

Received 23 October 2020 / Accepted 14 February 2021

ABSTRACT

Context. M dwarfs are key targets for high-resolution spectroscopy and model atmosphere analyses because of the high incidence of these stars in the solar neighbourhood and their importance as exoplanetary hosts. Several methodological challenges make such analyses difficult, leading to significant discrepancies in the published results.

Aims. The aim of our work is to compare M dwarf parameters derived by recent high-resolution near-infrared studies with each other and with fundamental stellar parameters. We also assess to what extent deviations from local thermodynamic equilibrium (LTE) for iron and potassium influence the outcome of these studies.

Methods. We carry out line formation calculations based on a modern model atmosphere grid appropriate for M dwarfs along with a synthetic spectrum synthesis code that treats formation of atomic and molecular lines in cool-star atmospheres including departures from LTE. We use near-infrared spectra collected with the CRIRES instrument at the ESO VLT as reference observational data.

Results. We find that the effective temperatures obtained with spectroscopic techniques in different studies mostly agree to better than 100 K and are mostly consistent with the fundamental temperatures derived from interferometric radii and bolometric fluxes. At the same time, much worse agreement in the surface gravities and metallicities is evident. Significant discrepancies in the latter parameters appear when results of the studies based on the optical and near-infrared observations are intercompared. We demonstrate that non-LTE effects are negligible for Fe I in M-dwarf atmospheres but are important for K I, which has a number of strong lines in the near-infrared spectra of these stars. These effects, leading to potassium abundance and metallicity corrections on the order of 0.2 dex, may be responsible for some of the discrepancies in the published analyses. Differences in the temperature–pressure structures of the atmospheric models may be another factor contributing to the deviations between the spectroscopic studies, in particular at low metallicities and high effective temperatures.

Conclusions. High-resolution spectroscopic studies of M dwarfs are yet to reach the level of consistency and reproducibility typical of similar investigations of FGK stars. Attention should be given to details of the line formation physics as well as input atomic and molecular data. Collecting high-quality spectra with a wide wavelength coverage of M dwarfs with known fundamental parameters is an essential step in benchmarking spectroscopic parameter determination of low-mass stars.

Key words. techniques: spectroscopic – stars: fundamental parameters – stars: atmospheres – stars: late-type – stars: low-mass

1. Introduction

M dwarfs have become a popular subject in the search for exoplanets and are targets for many current and upcoming missions from the ground as well as from space, such as CARMENES, TESS, PLATO, CRIRES+, SPIRou, and HARPS (Quirrenbach et al. 2010; Ricker et al. 2015; Rauer et al. 2014; Dorn et al. 2016; Donati et al. 2020; Mayor et al. 2003). This interest is due to the small mass and radius of M dwarfs and their low luminosity, which makes it easier to find planets around them using transit and radial-velocity methods. In addition, the likelihood of finding a planet in the habitable zone is larger around an M dwarf because the habitable zone is located closer to the star. It is estimated that each M dwarf has over two planets with a radius of between 1 and 4 $R_\oplus$ (Dressing & Charbonneau 2015). Over 650 planets have been found around M dwarfs so far[1]. M dwarfs also constitute over 70% of the stars in the solar neighbourhood (Henry et al. 2006) and are important for the study of the evolution of the elements in the Galaxy due to their long lifespan.

In order to determine the habitability of planets around M dwarfs, the parameters and abundances of the host star must be accurately determined. Additionally, the abundances in the photosphere of a main sequence star are believed to be a good indicator of the material from which both star and planets were formed (e.g. Thiabaud et al. 2015; Dorn et al. 2017). Accurately determining atmospheric parameters and abundances will advance theories on both planet formation and Galactic evolution.

However, the spectroscopic analysis of M dwarfs is challenging because the low temperatures cause the optical spectra to be riddled with molecular lines. Lines from titanium oxide increase in strength until mid-type M-dwarfs, and vanadium oxide bands are stronger in later types. Molecular lines from water are found at near-infrared wavelengths for mid- to late types (Gray & Corbally 2009). In general there are fewer molecular lines in the near-infrared and we can find isolated unblended atomic lines of several elements. However, these wavelength regions are contaminated by telluric lines when observing from the ground. The

[1] Number obtained from NASA exoplanet archive filtering by $T_{\rm eff}$ between 2300 and 3900 K and stellar radius between 0.10 and 0.56 $R_\odot$, September 2020. https://exoplanetarchive.ipac.caltech.edu/

multitude of molecular lines also makes it difficult to determine the level of the continuum flux needed for spectral analyses. Most M dwarfs are also highly convective. It is estimated that between 0.3 and 0.4 $M_{\odot}$ they become fully convective, which facilitates generation of strong magnetic fields (Browning 2008; Yadav et al. 2015). Magnetically sensitive lines are split due to the Zeeman effect which causes a broadening and intensification of the lines. The severity of the split is proportional to the magnetic field strength and the so-called Landé factor and M dwarfs have a stronger magnetic field than Sun-like stars by two to three orders of magnitude (Reiners 2012). The faintness is another problem requiring long exposure times for spectroscopic observations.

In recent years there has been significant progress in spectroscopic studies of M dwarfs. Abundance analysis is made possible with high-resolution near-infrared spectra obtained with modern spectrographs together with techniques for removing telluric lines. By avoiding magnetically sensitive lines, we can accurately determine stellar atmospheric parameters and abundances of individual elements. Recent studies include Lindgren et al. (2016, hereafter L2016), Lindgren & Heiter (2017, hereafter L2017), Veyette et al. (2017), Passegger et al. (2018, hereafter P2018), Passegger et al. (2019, hereafter P2019), Kuznetsov et al. (2019), Rajpurohit et al. (2018, hereafter R2018), López-Valdivia et al. (2019), Souto et al. (2020), and Birky et al. (2020). The parameters derived in these studies do not always agree, calling for detailed investigations of the different assumptions and methods used in these studies.

Other observational techniques can constrain the stellar parameters and give a model-independent reference value. Interferometry is one such important technique and with modern interferometers Boyajian et al. (2012) and Rabus et al. (2019) determined angular diameters for a small number of M dwarfs. With a known radius, a bolometric flux obtained with photometry, and distance from astrometry the Stefan-Boltzmann law is used to determine the effective temperature ($T_{\rm eff}$), and mass–luminosity relations are used to determine the surface gravity ($\log g$). However, the small angular sizes of M dwarfs present a challenge to the capabilities of modern interferometers, making it difficult to determine precise angular diameters of M dwarfs and to obtain $T_{\rm eff}$ independently from spectroscopy. Asteroseismology is another valuable technique to obtain stellar parameters such as mass and radius but much is unknown about pulsations in M dwarfs, making it difficult to use this method. Rodríguez-López (2019) give a review of the literature on observing pulsations in M dwarfs.

There is a need for benchmark M dwarfs that can be used for calibrations (sometimes called calibration stars). Pancino et al. (2017) present stars that were chosen as benchmark or calibrator stars for the *Gaia*-ESO survey (Gilmore et al. 2012; Randich et al. 2013). These included six M dwarfs (GJ 205, GJ 436, GJ 526, GJ 551, GJ 581, GJ 699, and GJ 880), three of which are part of the sample being discussed later in this paper. According to Pancino et al. (2017), the benchmark stars should have known parallaxes, which today can be easily obtained from the *Gaia* catalogue (Gaia Collaboration 2016, 2018), angular diameters, bolometric fluxes, and homogeneously determined masses. From these properties, effective temperature and surface gravity can be determined independently from spectroscopy and then be used to test the spectroscopic methods.

One possible reason for the discrepancies between derived parameters mentioned above could be departure from local thermodynamic equilibrium (LTE), that is, non-LTE effects. In this regard, apart from the effects on iron (the usual proxy for overall metallicity), it is interesting to consider departures in K I lines. This species is known to suffer from strong non-LTE effects in optical lines in FGK-type stars (Reggiani et al. 2019). However, there is less literature available on the effects on infrared lines in M dwarfs. There has been a general lack of investigations into non-LTE effects for M dwarfs. Of the studies compared in this paper, none used non-LTE calculations. L2016 and L2017 avoided potassium lines because these showed inconsistencies during the spectroscopic analysis. P2019 state that their model does not properly fit the core of the observed K I lines in the near-infrared. R2018 give no information regarding non-LTE or the fit of potassium lines. The other studies are not discussed in this paper. A possible explanation for the poor fit of K I lines could be non-LTE effects.

Despite the challenges, some authors, such as Neves et al. (2014) and P2018, determined parameters using spectra obtained in the optical. Others used optical combined with near-infrared, such as P2019, and R2018. In this paper we compare the derived parameters between high-resolution spectroscopic studies focusing on the near-infrared using similar methods. In the case of $T_{\rm eff}$, we compare with other methods such as interferometry. In this way, the model dependence can be explored and the spectroscopic methods can be improved. We focus on the studies by L2016, L2017, P2018, P2019, and R2018. We also explore possible reasons for discrepancies. L2016, L2017, P2018, and P2019 used similar methods and determined $\log g$ separately from fitting in order to break degeneracies between metallicity and surface gravity, while R2018 included $\log g$ in the fitting. For a comparison between high- and low-resolution spectroscopic studies we refer to the above-mentioned works, which compared their results to those of Mann et al. (2015) and Rojas-Ayala et al. (2012), among others. In Sect. 2 we discuss the studies and compare their parameters. In Sect. 3 we present a study of non-LTE effects in M dwarfs. In Sect. 4 we look into how the different parameters affect synthetic spectra and discuss to what extent non-LTE effects can explain the discrepancies in parameters. We also speculate on other possible reasons for the discrepancies. We end with our conclusions in Sect. 5.

2. Assessment of previous high-resolution studies of M dwarfs

2.1. Observations and analysis methods

The M dwarfs compared in this paper are from the sample of stars used in L2016 and L2017, which are also used in P2018, P2019, and R2018. The sample comprises 11 stars covering a range from early to mid M dwarfs. The stars and their spectral types can be found in Table 1.

The parameters from L2016 and L2017 were derived using observed spectra in the J band obtained with the original CRIRES spectrograph at ESO-VLT with a resolving power of $R \sim 50\,000$. The signal-to-noise ratio (S/N) of the spectra is given in Table 1. The parameters from P2018 and P2019 were derived using observed spectra obtained by the CARMENES instrument mounted at the Zeiss 3.5 m telescope at Calar Alto Observatory. The CARMENES instrument consists of two spectrographs covering the visible (520–960 nm) and near-infrared (960–1710 nm) wavelength range with a spectral resolution of $R \sim 94\,000$ and $R \sim 80\,500$, respectively. In P2018 only the visual wavelength range was used while in P2019 both visual and near-infrared were used separately as well as combined. These spectra have a S/N larger than 75. R2018 used both optical and near-infrared publicly available spectra from CARMENES.

Table 1. Stars in the sample with signal-to-noise ratio from L2016 and L2017, as well as spectral type from Simbad (Wenger et al. 2000).

Star	S/N	Sp. type
1 GJ 176	70	M2.5
2 GJ 179	150	M2
3 GJ 203	65	M3.5
4 GJ 436	140	M3
5 GJ 514	90	M1.0
6 GJ 581	140	M3
7 GJ 628	130	M3
8 GJ 849	90, 120	M3.5
9 GJ 876	100	M3.5
10 GJ 880	175	M1.5
11 GJ 908	125	M1

These spectra consist of a single exposure (Reiners et al. 2018) and thus have a lower S/N than the co-added spectra used by P2018 and P2019.

L2016 and L2017 used the software package Spectroscopy Made Easy, `SME`, (Valenti & Piskunov 1996; Piskunov & Valenti 2017) with `MARCS` (Gustafsson et al. 2008) atmospheric models included in `SME` to derive the stellar parameters. `SME` computes synthetic spectra on the fly based on a grid of model atmospheres and a line list containing atomic and molecular data. The parameters that are searched for are set as free parameters and χ^2 minimisation is used between the synthetic spectra and the observed spectra to find the best fit. The observations from CRIRES only cover a small wavelength range and there were too few atomic lines for L2016 and L2017 to simultaneously determine effective temperature, surface gravity, and metallicity. The effective temperature and surface gravity were therefore determined prior to the metallicity. L2016 and L2017 determined the effective temperature using fitting of FeH lines. However, this method was only applicable to mid M dwarfs, because for warmer, earlier types a degeneracy was found between temperature and metallicity. Because of this degeneracy, L2017 used temperatures from Mann et al. (2015) for the warmest stars (GJ 514, GJ 880, and GJ 908). For the surface gravity, L2016 used a $\log g$–mass relation from Bean et al. (2006) and L2017 used a mass–luminosity relation from Benedict et al. (2016) and radii from empirical relations from Mann et al. (2015). For the metallicity determination, L2016 and L2017 fitted lines of Fe, Ti, Mg, Ca, Si, Cr, Co, and Mn in `SME`, with metallicity and macroturbulence as free parameters. The projected equatorial rotation velocity $v \sin i$ was set to previous determinations from the literature or to a default value of 1 km s^{-1}. The microturbulence was set to a default value of 1 km s^{-1} in L2016, while fixed values based on predictions of published 3D radiation hydrodynamics calculations were used in L2017.

In P2018 and P2019, grids of synthetic spectra based on `PHOENIX` atmospheric models were used (ACES and SESAM, see Sect. 4.2). Because of a degeneracy between T_{eff}, $\log g$, and [Fe/H], $\log g$ was determined using evolutionary models and T_{eff} – $\log g$ relations. In P2018, Baraffe et al. (1998) was used and in P2019 they used the PARSEC v1.2S library (Bressan et al. 2012; Chen et al. 2014). The $v \sin i$ values were obtained from Jeffers et al. (2018) in P2018 and from Reiners et al. (2018) in P2019. For the microturbulence (v_{mic}), P2018 and P2019 used the relation $v_{\text{mic}} = 0.5 \cdot v_{\text{conv}}$, where v_{conv} is the convective velocity (which can also be seen as the macroturbulence) obtained from the atmospheric models (Passegger et al. 2016). For the fitting procedure, P2018 and P2019 used the γ-TiO band head and lines of K, Ti, Fe, and Mg, as well as Ca (P2019 only). For more information about the methods the reader is directed to P2018 and P2019.

R2018 fitted the whole wavelength region with synthetic spectra using BT-Settl model atmospheres based on the PHOENIX radiative transfer code (Allard et al. 2013). T_{eff}, $\log g$, and [M/H] were all fitted simultaneously. The fitted lines were Ti, Fe, Al, Ca II, K, Na, Mg, and OH.

2.2. Inferred stellar parameters

The stellar atmospheric parameters derived by L2016, L2017, P2018, P2019, and R2018 can be found in Table A.1. We show the different parameters in Fig. 1, where the stars are numbered as in Tables 1 and A.1. The results obtained for different wavelength regions (visual and/or near-infrared) by P2019 are shown separately. The left panel shows the effective temperatures. Most of the measurements agree within uncertainties, although there are some outliers. GJ 849 (number 8) is one such star for which P2019 determined an effective temperature of 3633 K in the near-infrared, which is significantly higher than all others. The derived temperature from L2016 is lower (3350 K) than the others which have temperatures above 3400 K. For all stars in the sample the general trend is that the effective temperatures from P2018 and P2019 are higher than those for L2016, L2017, and R2018, except for GJ 203 (star number 3). We can also see that for the cooler stars, P2018V has among the highest temperatures. We note that R2018 derived the same temperature for star numbers six and eight.

The middle panel of Fig. 1 shows $\log g$, and here we see a larger spread. The $\log g$ values derived in P2018 are often higher than those derived in L2016 and L2017, while the $\log g$ derived in P2019 tends to be lower. The method of determining $\log g$ was improved between P2018 and P2019. The $\log g$ values from P2019V are closer to L2016 and L2017 than those from P2019N and P2019NV. The general trend is that the surface gravities from R2018 are higher than those derived in the other studies for almost all stars. One exception is star number 4 (GJ 436) for which R2018 gives a surface gravity of 4 log cm s^{-2}; we note that this is outside the plot. For most of the cooler stars in the sample the surface gravity from R2018 appears to be within the uncertainty in comparison with the other studies (star number 2, 3, 6, 7, and 9). Important to note is that R2018 determined T_{eff}, $\log g$, and [M/H] simultaneously. There might therefore be some degeneracy between the parameters.

The right panel of Fig. 1 shows the metallicity. Also here we see a larger spread than for the effective temperature, and all values from P2018 and P2019 are more grouped around solar metallicity. Figures 5–7 in P2019 show a similar trend whereby their metallicities are shifted towards higher values compared to others found in the literature. Metallicities from R2018 are spread over the whole parameter range of the plot and the stars have in many cases a metallicity outside of the given uncertainties compared to the other studies. R2018 find higher metallicities than P2019 in most cases (excluding P2019N). Two clear exceptions are star numbers 4 and 5 (GJ 436 and GJ 514) which have significantly lower metallicites. GJ 436 also shows a discrepancy with the surface gravity. The metallicities found by R2018 are more extreme than the other derived metallicities. For many of the stars, R2018 find metallicities the magnitudes of which are outside of 0.3 [dex] while the other studies are inside of this range. Figure 1 also shows that the metallicities determined in the near-infrared by P2019 are generally higher than

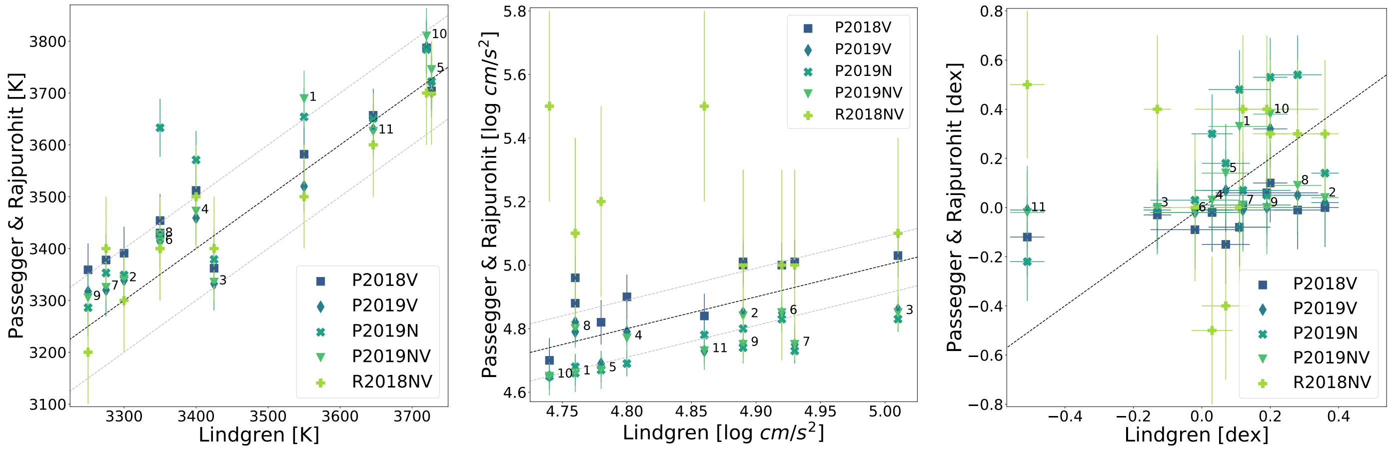

Fig. 1. Effective temperature (*left*), surface gravity (*middle*), and metallicity (*right*) derived for stars in common in Lindgren et al. (2016) and Lindgren & Heiter (2017) on the *x*-axis and Passegger et al. (2018, 2019); Rajpurohit et al. (2018) on the *y*-axis. See Table A.1 for star numbers and parameter values. The different symbols, designated V, N, and NV in the legend, indicate the wavelength regions (visual, near-infrared, and both combined) with which P2018, P2019, and R2018 derived the parameters. Error bars indicate corresponding uncertainties. The grey dashed lines indicate the mean uncertainties from L2016 and L2017 for the temperature and gravity. The black dashed diagonal line indicates a 1:1 relation. In the middle plot, showing surface gravity, the R2018 value for star number 4 is outside of the range of the plot. It has a surface gravity of 4 log cm s^{-2}.

the other determined metallicites by P2018, P2019, L2016, and L2017, while the P2018 metallicities are among the lowest. There are some outliers: GJ 179 (star number 2), GJ 203 (star number 3), GJ 849 (star number 8), and GJ 908 (star number 11). For GJ 849, P2018 and P2019 find a large spread in metallicity and for two of the values determined by P2018, P2019, and L2016, the difference in metallicity is larger than the quoted uncertainties. R2018 has a metallicity close to what was derived by L2016 for this star. For GJ 203, P2018, P2019, and L2017 agree while R2018 find a much higher metallicity outside of the given uncertainties. This can be connected with degeneracy mentioned above. For GJ 179 and GJ 908, the differences between the metallicities taken from P2018 and P2019 and taken from L2017 are also larger than the quoted uncertainties. The effective temperatures for both of these latter stars agree within uncertainties for all studies, as does the surface gravity for GJ 179. R2018 obtained a metallicity 1 dex higher for GJ 908 than what was derived by L2017. GJ 908 was discussed as an outlier in P2019 as well. The authors suggested that the reason for this might be that the star is a member of the thick disk with an older age than that assumed for the evolutionary models that were used to calculate log g. This cannot explain the large difference in metallicity because their $T_{\rm eff}$ and log g agree with those determined by L2017. L2017 did not use fitting of FeH lines for this star because it is a warm star and temperatures from Mann et al. (2015) were used. Rojas-Ayala et al. (2012) obtained an effective temperature of 3995 ± 47 K and an overall metallicity of −0.41 dex by investigating equivalent widths from low-resolution *K*-band spectra for the same star. Mann et al. (2015) obtained a metallicity of −0.45 dex and a $T_{\rm eff}$ of 3646 K using spectrophotometric calibrations. More high-resolution observations of this star are needed to accurately determine its atmospheric parameters.

The large discrepancies between values for surface gravity and metallicity that can be seen between R2018 and L2016, L2017, P2018, and P2019 can partly be explained by the difference in method and the quality of the observed data. R2018 used observed spectra from single exposures while P2018 and P2019 used co-added spectra which leads to higher S/N. L2016, L2017, P2018, and P2019 tried to break degeneracies by determining the surface gravity using empirical calibrations while R2018 determined all three parameters through fitting of synthetic spectra. Investigating the degeneracies between the parameters is outside the scope of this paper and therefore no further detailed comparison is done with R2018 in Sect. 4.

2.3. Comparison against interferometry

To further investigate the validity of the derived effective temperature, a comparison was done with a method that is independent of spectroscopy. Rabus et al. (2019) determined the effective temperature using interferometric measurements of the stellar disk from the VLT interferometer and photometry from the literature. In Rabus et al. (2019), the effective temperature can be found for 6 of the 11 stars that are being compared here, namely GJ 176, GJ 436, GJ 581, GJ 628, GJ 876, and GJ 880. The temperatures for these six stars are shown in the upper panel of Fig. 2 together with some additional stars found in Rabus et al. (2019) and L2016, L2017, P2018, P2019, and R2018. The differences in effective temperature for the six stars can be seen in the lower panel of Fig. 2.

For all but two stars, P2018 and P2019 determine a higher temperature than the interferometrically determined temperatures, regardless of whether the temperature was derived using optical or near-infrared wavelengths. The exceptions are GJ 176 and GJ 628 for which the interferometric temperatures are higher. We can see that the $T_{\rm eff}$ values from L2016 and L2017 generally tend to be similar to the interferometric ones, although slightly lower. For the same two stars, GJ 179 and GJ 628, the difference are significantly larger. R2018 also agrees with Rabus et al. (2019) within uncertainties for the six stars, with one exception which is the same star as mentioned before, GJ 176. In the upper panel of Fig. 2 we can see that R2018 see a larger spread in effective temperatures than the other studies when comparing to Rabus et al. (2019).

Rabus et al. (2019) compare their effective temperatures with those derived by Neves et al. (2014) who used high-resolution optical spectra and find that the effective temperatures from the optical by Neves et al. (2014) are overestimated compared to the

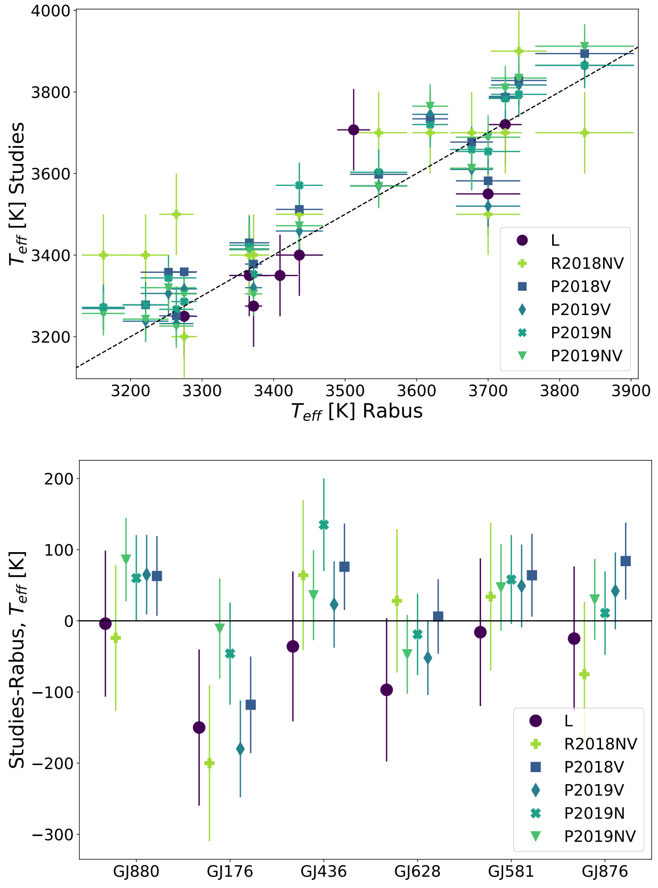

Fig. 2. *Top*: effective temperatures for a sample of stars from Passegger et al. (P2018 and P2019), Rajpurohit et al. (R2018), and/or Lindgren et al. (L2016 or L2017, designated L) that overlaps with the sample from Rabus et al. (2019). *Bottom*: difference in effective temperature for the six stars in common between Lindgren et al., Passegger et al., Rajpurohit et al., and Rabus et al. (2019). The temperature from Rabus et al. (2019) was subtracted from the others. The error bars indicate the combined uncertainties. V, N, and NV have the same meaning as in Fig. 1.

near-infrared interferometric effective temperature. It is not clear from Fig. 2 that the effective temperatures obtained from spectra in the optical are higher than those obtained in the near-infrared. When looking at the standard deviation of the difference between $T_{\rm eff}$ values for all stars we find that the data coming from the optical have a higher standard deviation than the others, excluding R2018 (70 K for P2018V and 85 K for P2019V versus 52 K for L, 59 K for P2019N, and 42 K for P2019NV). R2018 uses the whole wavelength range and has a standard deviation of 89 K. Parameters derived in the optical also have among the highest absolute mean difference (69 K for both P2018V and P2019V versus 55 K for L and P2019N, 43 K for P2019NV). R2018 has a mean difference of 71 K. The combined optical and near-infrared wavelength range from P2019 gave the lowest standard deviation and mean difference while R2018 has the highest. This can indicate that it is better to use near-infrared or combined optical and near-infrared than optical spectra alone. However, this sample is too small to come to a definitive conclusion. The deviating results of R2018 cannot be taken into account in this regard because they are based on observations of lower quality and a fundamentally different method for determining $\log g$. More interferometric observations of M dwarfs are needed so that derived temperatures can be compared to spectroscopically independent temperatures.

3. Non-LTE effects in M dwarfs

One aspect that can affect the spectroscopic analysis is departure from LTE, that is, non-LTE effects. This has not yet been investigated in-depth in the case of M dwarfs. Non-LTE effects can deepen the cores of some lines for some elements and weaken them for other elements as well as affect the wings. Neglecting non-LTE will affect spectroscopically derived parameters and chemical abundances. Recent examples of non-LTE studies of potassium including K dwarfs are provided by Reggiani et al. (2019) and Korotin et al. (2020). Non-LTE effects of iron in late-type stars are discussed in Lind et al. (2012).

Reggiani et al. (2019) investigated non-LTE effects for three optical and one near-infrared K lines in six stars. The coolest star in the sample was a K dwarf. For all stars in their sample there was a clear difference in line strength between LTE and non-LTE for the resonance line at 7699 Å. Differences were also found for the other lines, although these were significantly smaller than for the resonance line. For the K dwarf, an abundance difference of −0.23 dex between LTE and non-LTE for the resonance line was determined. Lind et al. (2012) investigated non-LTE effects of Fe in late-type stars. In their Fig. 2 we can see that for 4000 K, a surface gravity of 4.5, and solar metallicity, the difference in abundance for the lines studied by the authors is smaller than 0.01 dex.

Non-LTE effects were not included in L2016 and L2017. The synthetic spectra used by P2018 included non-LTE for some species for effective temperatures above 4000 K (Husser et al. 2013), and we assume that non-LTE is treated in the same way in the model grid used by P2019, which indicates that the analysis was done in LTE in both cases (see Sect. 4.2). P2019 state that the core of the K I lines could not be fitted properly. Neither R2018 nor Allard et al. (2013) give any information regarding non-LTE, so we assume that their calculations were done in LTE. In this section we analyse the non-LTE effects in M dwarfs for K I and Fe I. Other species will be investigated in later papers.

3.1. Method

We used the line formation code Spectroscopy Made Easy (`SME`; Valenti & Piskunov 1996; Piskunov & Valenti 2017) version 553 with atmospheric models from the standard `MARCS` grid (Gustafsson et al. 2008) and solar abundances from Grevesse et al. (2007). Atomic and molecular (OH, MgH, TiO) data were extracted from the `VALD` database[2] (Piskunov et al. 1995; Ryabchikova et al. 2015) in a wavelength range from 10 000 to 16 000 Å and around the K I resonance line at 7699 Å using the default configuration and the Extract Stellar tool with the following stellar parameters: $T_{\rm eff}$ = 3000 K, $\log g$ = 4 [cm s^{-2}], and solar abundances from Grevesse & Sauval (1998) enhanced by +0.5 dex. Data for the most important lines in the wavelength regions investigated below are given in Tables B.1 and B.2.

`SME` takes departures from LTE into account by interpolating pre-computed grids of departure coefficients. Details of this can be found in Sect. 3 of Piskunov & Valenti (2017). For potassium, departure coefficient grids were adopted from Amarsi et al. (2020). These were calculated using the model atom of Reggiani et al. (2019), extended down to $T_{\rm eff}$ = 3000 K and up to $\log g$ = 5.5 dex. For iron, we adopted grids from Amarsi et al. (2016), extended down to $T_{\rm eff}$ = 3500 K and up to $\log g$ = 5.0 dex. Both go down to [Fe/H] = −5; the iron grid extends up to [Fe/H] = +0.5, the potassium grid up to [Fe/H] = +1.0.

[2] http://vald.astro.uu.se

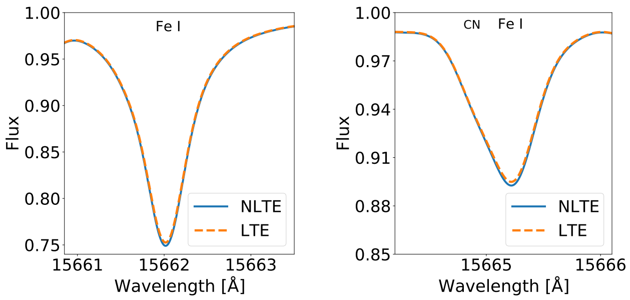

Fig. 3. Line profiles for two Fe lines in LTE and non-LTE (NLTE). We highlight the difference in scale on the *y*-axis. The lines were generated with $T_{\mathrm{eff}} = 3500$ K, log $g = 4.6$, and [M/H] = 0.5 dex. The weaker line to the right is blended by CN in the blue wing. No observed spectra were available for comparison.

3.2. Effects on Fe I lines

For iron we generated a small grid of synthetic spectra covering a wavelength range of 10 000–16 000 Å, with T_{eff} 3500 and 3800 K, log g 4.6 and 4.9, and metallicity 0.5 and −0.5 dex, both in LTE and non-LTE. We observed the largest difference between LTE and non-LTE for the lowest temperature, highest metallicity, and lowest gravity. In Fig. 3 we show two example Fe I line profiles generated for the set of parameters showing the largest difference. These lines are among the lines most affected by non-LTE in the near-infrared. As can be seen in the figure, the non-LTE line is marginally deeper than the LTE line. The differences in line depth between LTE and non-LTE are 0.48% for the line at 15 662 Å and 0.26% for the line at 15 665 Å. The difference in equivalent width between LTE and non-LTE for the stronger line is 1.7% and for the weaker line is 2.0%. The abundance difference between non-LTE and LTE for both of these lines is 0.018 dex. This was found by generating synthetic spectra in SME where the Fe I abundance was altered so that the equivalent width of the non-LTE line matched that of the LTE line. The non-LTE abundance had to be lowered because the LTE lines are weaker in the core. The difference for Fe I between LTE and non-LTE is very small for M dwarfs, which is in accordance with the study by Lind et al. (2012). On the contrary, we found that the non-LTE effect increased with decreasing effective temperatures while Lind et al. (2012) found that it increases with increasing effective temperature. As the largest difference between LTE and non-LTE occurred for the lowest temperature, it is possible that the non-LTE effect in iron will increase when going to even cooler M dwarfs. A grid of departure coefficients extending to lower temperatures is needed to explore this.

3.3. Effects on K I lines

Synthetic spectra were generated in the wavelength range 10 000 to 16 000 Å in LTE and non-LTE with parameters from L2017 for the stars GJ 179, GJ 203, GJ 514, GJ 880, and GJ 908 (see Table A.1) and then compared. These stars were chosen as they represent both low and high effective temperatures, as well as different metallicities. All of these stars were investigated in L2017 and the observed spectrum used in this comparison is the same as the one used in L2017. The K lines in the near-infrared most affected by non-LTE can be seen in Table 2, which also shows the percentage difference between the equivalent width in LTE and non-LTE as well as the reduced equivalent width for the stars with the strongest and weakest lines. In Fig. 4 we show the line profiles of two of the K lines in LTE and non-LTE for three stars (GJ 179, GJ 203, and GJ 880). As can be seen in the figure, the non-LTE lines are significantly deeper than the LTE lines and better match the observed lines. This is in accordance with theory which states that non-LTE effects for K are mostly driven by photon losses which generate an overpopulation in the lower energy levels of the transitions, making the lines deeper in non-LTE (Asplund 2005). The largest differences between LTE and non-LTE occur for the strongest lines in the near-infrared which also have the lowest transition energies; see Table 2. We also included the resonance line at 7699 Å which was examined in previous studies of non-LTE in FGK stars (Reggiani et al. 2019; Korotin et al. 2020). This line has a smaller difference in equivalent width than the lines in the near-infrared. The line is severely blended with TiO and the non-LTE line is saturated. The importance of the non-LTE effect on other potassium lines in optical spectra of M dwarfs is beyond the scope of this work and is left to be determined in future studies.

To further test the differences between LTE and non-LTE, an abundance analysis was performed for K for the same five stars as above. Individual K lines in the near-infrared were fitted one at a time by varying the abundance of K in SME using the parameters from L2017 (found in Table A.1). The fit was done against CRIRES-observed spectra in two small wavelength ranges (11 670–11 730 Å and 11 750–11 800 Å). The observed spectra are the same as those used in L2017. For these five stars, only three K lines are available in the observed spectra (one is strongly blended with an iron line). The abundance differences obtained in the fitting between non-LTE and LTE for these three lines can be seen in Table 3 (columns “Fit”).

As the observed spectra covered few K lines, we expanded the investigation to all K lines that showed a clear non-LTE effect in the near-infrared (as seen in Table 2), with the addition of the resonance line at 7699 Å used by P2018 and P2019. This was done by generating an LTE synthetic spectrum using SME with the same settings as in the previous test. We then generated non-LTE synthetic spectra and altered the abundance of K to match the equivalent width of the K lines in the LTE synthetic spectrum. We had to lower the non-LTE abundances in order to mimic the equivalent widths measured from the LTE spectrum. However, we emphasise that the line shapes of the LTE and non-LTE synthetic spectra were significantly different. Therefore, the abundance differences should be interpreted with caution. The result can be seen in Table 3 (columns “Eq wi”). The abundance correction derived from fitting is higher than the abundance correction obtained using equivalent widths. The reason for this is unknown. The three warmest stars (GJ 514, GJ 880, and GJ 908) show the largest difference between non-LTE and LTE. Korotin et al. (2020) present similar results as in Tables 2 and 3 for lines in the near-infrared for FGK stars. These latter authors find that the K I lines at 11 769 Å, 11 772 Å, 12 432 Å, and 12 522 Å need to be calculated in non-LTE while the lines at 15 163 Å and 15 168 Å can be treated in LTE.

We show the abundance corrections derived using equivalent widths for some of the K lines in Fig. 5. Each colour represents one potassium line and each symbol represents a star. In the upper panel we can clearly see that for the stronger lines at 11 769 and 12 432 Å the abundance correction increases with the effective temperature. The resonance line at 7699 Å has a similar correction for all temperatures, as does the weaker line at 15 163 Å. In the lower panel we can see how the abundance correction changes with metallicity. We see that for the two strong lines the abundance corrections are larger for 0.0 and 0.2 dex

Table 2. Difference in equivalent width between LTE and non-LTE for K lines in the near-infrared with wavelength λ.

λ [Å]	$E_{\rm low}$ [eV]	GJ 179 [%]	GJ 203 [%]	GJ 514 [%]	GJ 880 [%]	GJ 908 [%]	GJ 179 eq.w	GJ 908 eq.w
7699.0	0.000	−1.3	−2.4	−3.6	−2.9	−4.9	−3.47	−3.85
11 019.8	2.670	−1.1	−1.1	−1.4	−1.4	−0.6	−4.95	−5.79
11 022.6	2.670	−1.2	−1.1	−1.4	−1.6	−0.8	−5.09	−5.93
11 690.2	1.610	−4.9	−6.8	−8.5	−8.0	−7.8	−4.15	−4.39
11 769.6	1.617	−6.6	−9.2	−12.1	−11.3	−13.4	−4.49	−4.94
11 772.8	1.617	−5.9	−8.9	−12.9	−11.7	−13.7	−4.11	−4.50
12 432.3	1.610	−6.3	−9.1	−12.5	−11.5	−14.4	−4.39	−4.88
12 522.1	1.617	−5.5	−8.2	−11.0	−9.9	−12.0	−4.19	−4.61
13 377.8	2.670	−1.6	−0.2	−2.2	−1.2	...	−6.04	−6.83
15 163.1	2.670	−0.8	−0.6	−0.9	−0.9	−0.6	−4.39	−4.87
15 168.4	2.670	−0.8	−0.6	−1.0	−0.8	−0.6	−4.47	−5.02

Notes. The second column gives the energy of the lower level of the transition ($E_{\rm low}$). The last two columns show the reduced equivalent width calculated from the LTE synthetic spectra for GJ 179 and GJ 908, which have the strongest and the weakest lines, respectively. The differences in equivalent width are calculated as (LTE−non-LTE)/non-LTE·100. The K I line at 13 377.8 Å in the star GJ 908 was too weak for the measurement of equivalent widths. The reduced equivalent widths are calculated by $\log(\text{eq.width}_{\rm LTE}/\lambda)$.

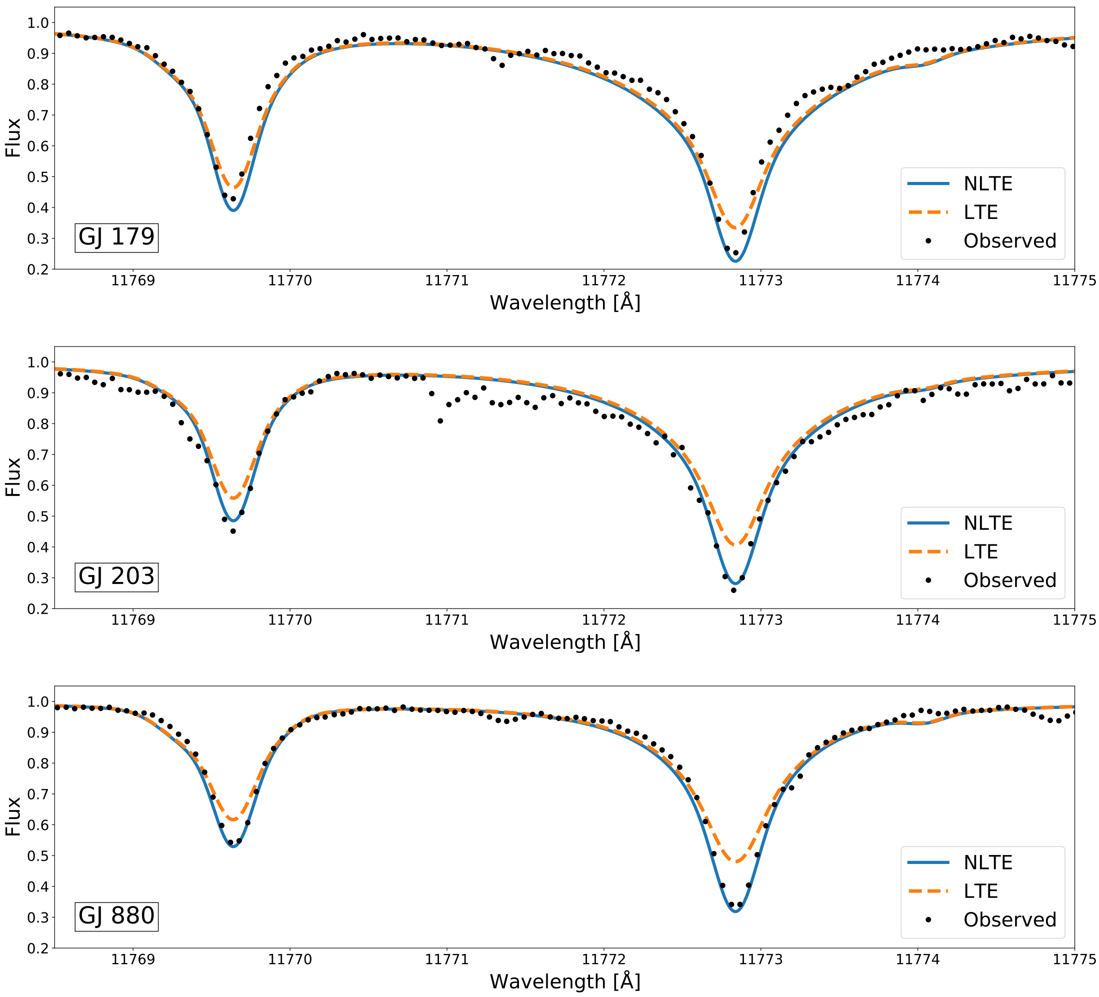

Fig. 4. Synthetic spectra showing two K lines generated with parameters for GJ 179, GJ 203, and GJ 880 by L2017 in LTE and non-LTE (NLTE) (dashed orange and solid blue lines, respectively). The black points shows the observed spectrum for reference. The observed spectrum for GJ 203 has a lower S/N than the other observed spectra.

than for the other metallicities. The two stars corresponding to these points are the two warmest stars. Thus it seems that the non-LTE effects vary more with effective temperature than with metallicity.

Asplund (2005) states that, for the resonance line, the largest abundance correction between LTE and non-LTE occurs for the highest effective temperatures and lowest surface gravities. We observe that the two warmest stars (GJ 514 and GJ 880) in

Table 3. Abundance corrections (differences in abundance for non-LTE−LTE in dex) for K lines determined by matching the equivalent widths (columns "Eq wi") and fitting the line profiles (columns "Fit") of K lines at wavelength λ.

λ [Å]	GJ 179		GJ 203		GJ 514		GJ 880		GJ 908	
	Eq wi	Fit	Eq wi	Fit	Eq wi	Fit	Eq wi	Fit	Eq wi	Fit
7699.0	−0.065	...	−0.060	...	−0.074	...	−0.069	...	−0.069	...
11019.8	−0.007	...	−0.005	...	−0.008	...	−0.008	...	−0.004	...
11022.6	−0.007	...	−0.005	...	−0.008	...	−0.009	...	−0.004	...
11690.2	−0.076	−0.108	−0.119	−0.138	−0.222	−0.372	−0.208	−0.270	−0.192	−0.258
11769.6	−0.085	−0.127	−0.104	−0.130	−0.157	−0.211	−0.157	−0.195	−0.119	−0.141
11772.8	−0.072	−0.077	−0.104	−0.089	−0.158	−0.165	−0.141	−0.137	−0.151	−0.203
12432.3	−0.074	...	−0.094	...	−0.134	...	−0.130	...	−0.107	...
12522.1	−0.061	...	−0.089	...	−0.140	...	−0.126	...	−0.118	...
13377.8	−0.006	...	−0.004	...	−0.006	...	−0.009	...	−0.004	...
15163.1	−0.009	...	−0.006	...	−0.008	...	−0.009	...	−0.004	...
15168.4	−0.008	...	−0.005	...	−0.007	...	−0.008	...	−0.004	...

Notes. The line at 11 690.2 Å is blended with Fe I.

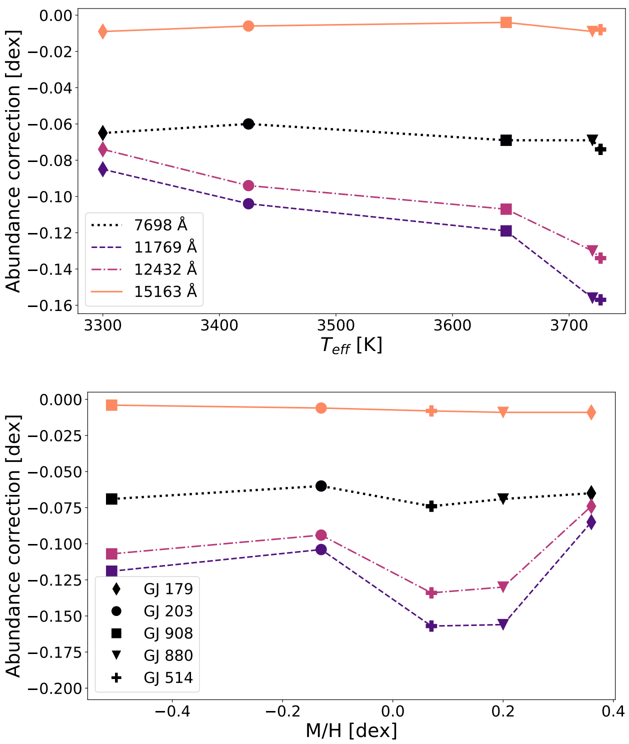

Fig. 5. Abundance corrections for four different potassium lines from Table 3 versus effective temperature and metallicity for the stars in the table. The legend in the top panel shows the line styles used to indicate different spectral lines, and the legend in the lower panel shows the symbols used to indicate different stars.

Table 2 also have among the lowest surface gravities of the sample. The abundance corrections for these stars are among the highest.

3.4. Effects on inferred stellar parameters

In order to estimate how non-LTE would affect the spectroscopically derived parameters by L2016, L2017, P2018, P2019, and R2018 we investigated the differences in $T_{\rm eff}$ and metallicity obtained when LTE is used for fitting K lines compared to when non-LTE is used. In P2018, one out of 15 lines was K I, while in P2019, five out of 15 lines were K I in the wavelength region classified as near-infrared by the authors. L2016 and L2017 avoided K I lines. R2018 use several K lines but these represent a smaller fraction than those in P2019. As a considerable number of near-infrared potassium lines were used in P2019 it is important to estimate how non-LTE would affect the parameters derived in this case. We fitted a synthetic spectrum to an observed spectrum using SME, with $T_{\rm eff}$ and metallicity as a free parameters (one at a time) for the same stars as in Sect. 3.3 in a short wavelength range including K lines in LTE and non-LTE (see Fig. 6). The other parameters were set to values from L2017; see Table A.1. As the non-LTE effects of Fe I were found to be minor, this species was fixed to LTE in all cases.

As can be seen in Fig. 6 there is a clear difference between non-LTE and LTE for the K lines but the difference is small for the other lines. In Table 4 we list the differences in $T_{\rm eff}$ and metallicity for the five stars. These differences should only be seen as indications of the possible non-LTE effect on the effective temperature and metallicity and not actual temperature and metallicity corrections for these stars. This is because only a short wavelength range was used. We find that LTE underestimates the effective temperature compared to non-LTE. For the coolest star (GJ 179), the effective temperature derived in non-LTE is 88 K higher than the LTE effective temperature, while for one of the warmest stars (GJ 880), the non-LTE effective temperature is 213 K higher. For the warmest star (GJ 514), the difference is 153 K. This indicates that the temperatures derived by P2018 and P2019 might be underestimated and that the discrepancy is larger for the warmer stars. This effect could be larger in P2019 because a larger number of K I lines were used in the fitting in the near-infrared. For R2018 temperatures, the effect would be similar to that seen for P2018 and P2019 but not as severe because R2018 use more lines from other elements in the fitting. We note that applying temperature corrections according to these considerations would increase the differences between the compared studies.

For the metallicity, we find that the LTE metallicity is higher than the non-LTE metallicity. The largest difference between LTE and non-LTE occurs for GJ 179 which is the coolest star of this sample and has the highest metallicity. The second-coolest star (GJ 203) shows the second-largest difference between LTE and non-LTE metallicity. This star has a low metallicity and the highest surface gravity in the sample. The two warmest stars (GJ 514 and GJ 880) have among the lowest surface gravities and show the lowest difference in metallicity between LTE and

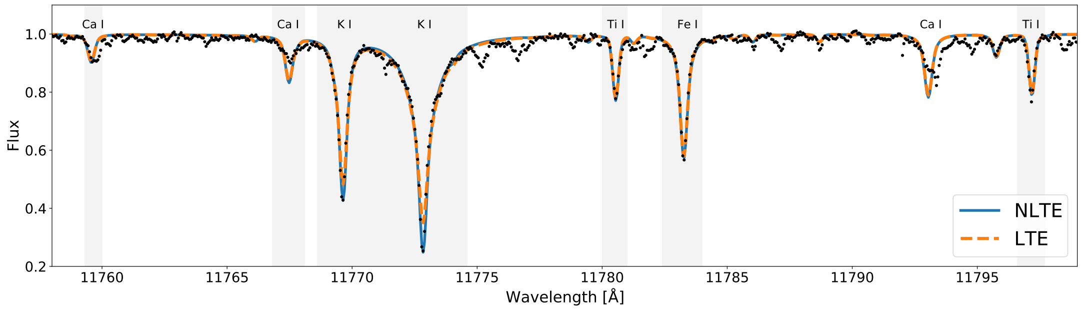

Fig. 6. Synthetic spectra for the star GJ 179 for best-fit $T_{\rm eff}$ in LTE and non-LTE (NLTE), dashed and solid lines respectively. Black points indicate the observed spectrum. Shaded areas show fitted regions.

Table 4. Difference in effective temperature and metallicity between non-LTE and LTE for five stars (non-LTE−LTE) derived from fitting synthetic to observed spectra in the wavelength region shown in Fig. 6.

Star	$\Delta T_{\rm eff}$ [K]	Δ [M/H] [dex]
GJ 179	88	−0.24
GJ 203	50	−0.20
GJ 514	153	−0.16
GJ 880	213	−0.15
GJ 908	133	−0.19

non-LTE. It is interesting to note that GJ 880 has a higher metallicity and shows a greater difference in $T_{\rm eff}$ than GJ 514 even though the two objects have similar effective temperatures. Lowering the metallicity in the P2019N (near-infrared) sample would decrease the difference between P2019N, and L2016 and L2017 for about half of the stars. Two of these stars were identified as outliers above (GJ 849 and GJ 908). For GJ 849, the metallicity from P2019N is much higher than the others. Lowering this metallicity would bring it more in line with the other results from P2018 and P2019, as well as that found by L2016. However, this star also has a discrepancy in the derived effective temperatures (see Sect. 2.2). For GJ 908, the metallicity from P2019N is closer to that found by L2017 than the other metallicity estimates from P2018 and P2019. Lowering it further would bring it more in line with that found by L2017, Rojas-Ayala et al. (2012), and Mann et al. (2015). However, this would increase the difference to the other metallicities from P2018 and P2019. Lowering the metallicity of R2018 would also decrease the difference between R2018, and L2016 and L2017 for about half of the stars. This is especially true for GJ 908 which shows a very large difference between R2018 and L2017. Two strong exceptions are GJ 436 and GJ 514 that were given as outliers in Sect. 2.

As mentioned in Sect. 2.2 the metallicities from P2019N are generally higher than the other metallicities and would therefore benefit the most from a downward correction of metallicity. When looking at Figs. 5 and 6 of P2019 we can see that increasing the effective temperatures of P2019 by 100–200 K would worsen the fit to the literature values while lowering the metallicity by 0.15 dex might improve it.

4. Possible explanations for parameter discrepancies

4.1. Comparing synthetic and observed spectra

In order to further investigate the difference in the derived atmospheric parameters we generated synthetic spectra in LTE using SME, MARCS atmospheric models, and the line list described in Sect. 3.1. In addition, the line data for FeH used by L2017 were added[3]. Solar abundances from Grevesse et al. (2007) were used. The parameters given in Table A.1 were used. Synthetic spectra were not generated with parameters from R2018 because of the differences in methods; see Sect. 2. For the synthetic spectra generated with the P2018 and P2019 parameters, the microturbulence was estimated from Fig. 3 in Husser et al. (2013) and for the macroturbulence the relation mentioned in Sect. 2.1 was used. We used the turbulences given in L2016 and L2017 for the corresponding parameters. The generated synthetic spectra were then compared to observed spectra obtained by the CRIRES spectrograph at the VLT (the same spectra were used in L2016 and L2017). There are spectra available from CARMENES (Reiners et al. 2018) with a lower S/N than that of the spectra used in P2018 and P2019 but the CARMENES spectra are also riddled with telluric lines; for this, reasons we do not include a comparison to these spectra in this investigation.

We made a χ^2 comparison of the cores of the strongest lines in the synthetic and observed spectra. A small wavelength region of ±0.1 Å around the minimum flux was investigated. The resulting values of reduced χ^2 for four of the stars and the 12 strongest lines are presented in Figs. 7–10. The central wavelengths of these lines and the observed fluxes at these wavelengths are listed in Table 5. The stars shown in the figures were selected to represent the different cases of agreement between the metallicities from L2016 and L2017, and P2018 and P2019, as follows. Two of the stars (GJ 179 and GJ 908) show metallicity differences that are larger than the uncertainties, with opposite signs. Good agreement is seen between the metallicities for GJ 203 and with a small spread, while on average good agreement is seen for the metallicities for GJ 176 but with a large spread. In the figures we also show the reduced χ^2 calculated in the same way between the observed and synthetic spectra, but generated with potassium in non-LTE for L2016, L2017, and P2019 parameters (open symbols). We did not calculate the reduced χ^2 for P2018 in non-LTE because the method was improved in P2019 (see Sect. 4.2). The straight lines in the figures are a visual aid and should not be seen as a prediction of intermediate values. The upper panels show the entire range of the reduced χ^2 and the lower panels focus on low values of χ^2. The y-scale is the same for all stars in the lower panels, except for GJ 179 which in general has larger χ^2 values.

The metallicities for GJ 176 from L2016 and P2019 agree within uncertainties and show a large spread. In Fig. 7 we see a spread in χ^2 for several lines. For GJ 179, the derived metallicities are outside of the combined uncertainties of the investigated studies and show a large spread. The reduced χ^2 values for

[3] Available on the MARCS webpage at `https://marcs.astro.uu.se/documents.php`

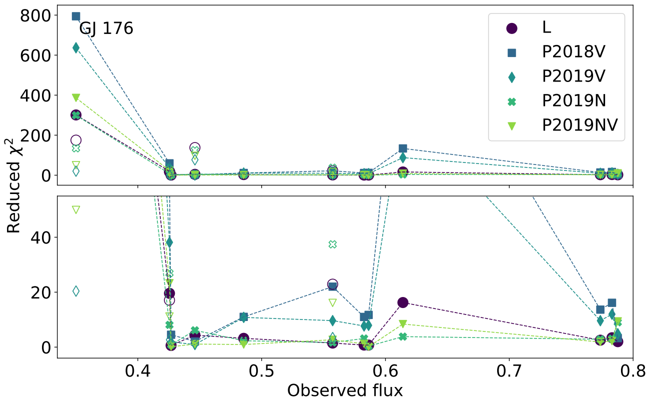

Fig. 7. Reduced χ^2 between the synthetic and observed spectra for the cores of the 12 strongest lines for the star GJ 176 as a function of the observed flux in the centre of the lines (filled symbols). The symbols are the same as in Fig. 2 and refer to the parameters used for the synthetic spectra. The upper panel shows the whole range of χ^2 while the lower panel focuses on χ^2 below 50. The open symbols indicate the χ^2 of K lines generated in non-LTE for L2016 or L2017 and P2019. The identifications of all lines are presented in Table 5 together with the wavelengths and observed fluxes.

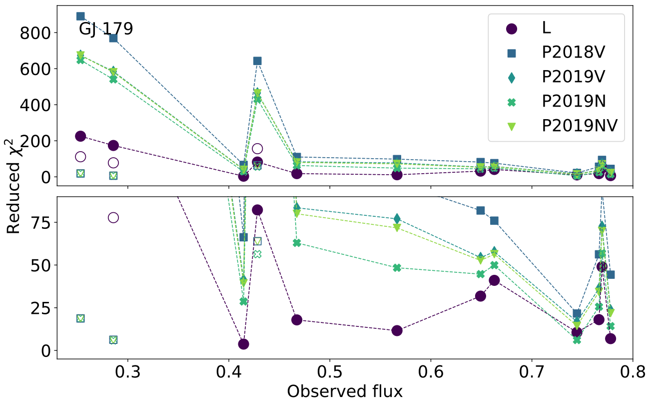

Fig. 8. Same as Fig. 7 but for the star GJ 179. The lower panel focuses on χ^2 below 90.

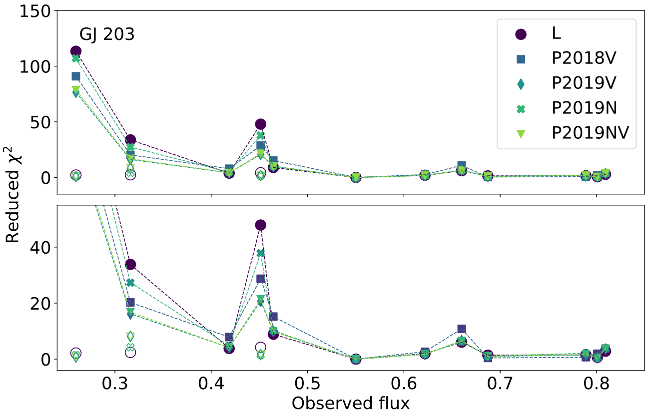

Fig. 9. Same as Fig. 7 but for the star GJ 203.

GJ 179 in Fig. 8 are generally larger than for any other star in this sample, and this star was given as an outlier in previous sections. In Fig. 9 (GJ 203), we see only small differences in the reduced χ^2 for all non-potassium lines. The metallicities derived

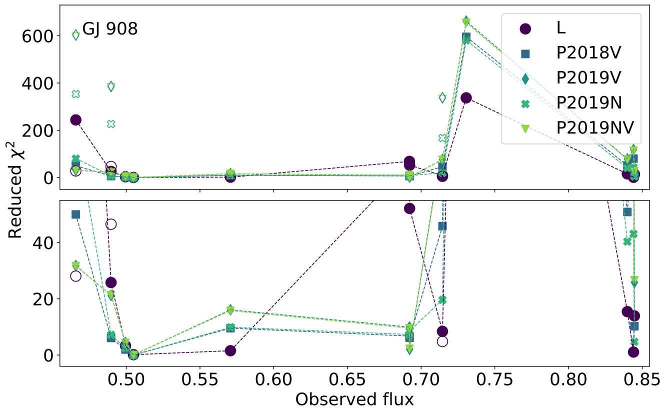

Fig. 10. Same as Fig. 7 but for the star GJ 908.

Table 5. Twelve strongest lines shown in Figs. 7–10.

		Observed flux			
Species	λ [Å]	GJ 176	GJ 179	GJ 203	GJ 908
Mg I	11 828.2	0.486	...	0.550	0.505
K I	11 690.2	0.350	0.286	0.316	0.490
K I	11 769.6	0.557	0.428	0.451	0.715
K I	11 772.8	0.446	0.253	0.260	0.466
K I	12 522.1	0.426	...	...	...
Ca I	13 033.6	...	0.745	0.789	0.844
Ti I	11 780.5	0.774	0.778	...	0.840
Ti I	11 797.2	0.783	0.766	0.809	...
Ti I	11 892.9	...	0.663	0.660	0.692
Ti I	11 949.5	0.614	0.649	0.687	0.692
Ti I	11 973.8	0.583	...	...	...
Ti I	13 011.9	...	0.769	0.801	0.845
Fe I	11 783.3	0.583	0.567	0.622	0.731
Fe I	11 882.8	...	0.415	0.419	0.500
Fe I	11 884.0	...	0.467	0.465	0.571
Fe I	11 973.0	0.427	...	...	...
Si I	12 031.5	0.788	...	...	...

Notes. The central wavelength and the observed flux at that wavelength are given. The K I line at 11 690.2 Å is blended with a Fe I line.

for this star also show a small spread and agree within uncertainties. Metallicities have been derived for GJ 908 that do not agree within the uncertainties and this star is a clear outlier in Fig. 1. The reduced χ^2 for GJ 908 (Fig. 10) also shows a spread, but this is not as large as for GJ 179. The χ^2 values for P2019 are smaller than for P2018 which indicates an improvement in the method between P2018 and P2019. For GJ 176 and GJ 179, L2016 and L2017 find a lower χ^2 than P2018 and 2019 for most of the lines in Figs. 7 and 8. For GJ 908, L2017 find a better fit, except for two Ti lines in the middle of Fig. 10. L2017, P2018, and P2019 agree for GJ 203.

At this point, we can state that there is an inconsistency between the parameters derived by the different authors, because we cannot reproduce a good fit to the observations with the method of L2016 and L2017 using parameters derived by P2018 and P2019. The parameters are clearly model dependent. However, we cannot say which of the models are more realistic because of the various assumptions made in the comparison, especially for the abundances of individual elements used when calculating the synthetic spectra. A change in the abundances could improve or worsen the fit to the observations for any of the parameter sets.

We can see that the majority of the lines with the largest χ^2 are K I lines. For most of the K I lines, the χ^2 improves when using non-LTE, although there are some exceptions. One is for the star GJ 176 (Fig. 7) where the fourth and sixth lines are K lines (with observed flux 0.446 and 0.557, respectively) for which LTE gives a lower reduced χ^2 than non-LTE. When visually comparing these lines, we see that the synthetic spectra generated in LTE show a better fit to the observed spectrum than the non-LTE spectra. Another exception is the fourth line in Fig. 8 (observed flux 0.428) where the L2017 line calculated in non-LTE has a χ^2 that is about twice that found for the respective LTE line. This line can be seen to the left in Fig. 4. All K lines improved when using P2019 parameters with non-LTE for this star. The star GJ 908 also shows lines that have a worse fit with K in non-LTE. The L2017 line for this star that has a poor fit (observed flux 0.490) is blended with Fe which can cause discrepancies. All K lines generated with parameters from P2019 show a worse fit in non-LTE than in LTE for GJ 908.

4.2. Comparison of model atmospheres

Discrepancies in derived parameters may not only be caused by non-LTE effects, but also by differences in other ingredients of the analysis, such as using different atmospheric models. In order to evaluate the effect of differences in atmospheric models we compare the model structures used by L2016, L2017, P2018, and P2019. L2016 and L2017 used MARCS atmospheric models (Gustafsson et al. 2008), while P2018 and P2019 based their analysis on PHOENIX models. The PHOENIX models used by P2018 and P2019 were of two different flavours, mainly differing in the equation of state (EOS) and the atomic and molecular line lists used. The models used by P2018 are presented in Husser et al. (2013) and are made available online (see below). P2018 use the ACES[4] EOS with thermodynamic data for hundreds of species, including about 250 molecules and over 200 condensates. The models applied by P2019 use the SESAM[5] EOS, which is discussed extensively in Meyer (2017). These models are not (yet) publicly available. Both ACES and SESAM calculate the chemical equilibrium based on the Villars-Cruise-Smith method (Smith & Missen 1982). The SESAM EOS was developed in order to enable the PHOENIX code to model Earth-like planetary atmospheres with effective temperatures of a few hundred K. This included an improved treatment of condensed species, together with improvements on the numerical side.

Meyer (2017) compared PHOENIX models calculated with both the ACES and the SESAM EOS for an effective temperature of 3000 K and concluded that both versions resulted in very similar atmospheric structures. A comparison of spectra calculated for M-dwarf parameters with PHOENIX using ACES and SESAM is provided in Fig. 2 of P2019. Deviations are mostly seen for individual atomic (Mg I, Ca II) and molecular (e.g. TiO) lines, which indicates that the differences are mainly due to different atomic and molecular data used. The model structures for M dwarfs are expected to be very similar for the two PHOENIX versions, given that the implemented improvements focused on a much lower temperature range.

Based on the above, we use the publicly available PHOENIX version (with the ACES EOS) for a comparison with MARCS models. In the computation of the MARCS models, a Newton-Raphson method was used to calculate the chemical equilibrium, including about 500 molecular species (Gustafsson et al. 2008). We note that when synthetic spectra based on MARCS models are calculated, SME uses its own EOS to re-calculate the chemical equilibrium and the partial pressures, including electron pressure (also based on a Newton-Raphson method; see Piskunov & Valenti 2017) for atoms and ions, and about 200 molecular species.

Both of the atmospheric model codes assume LTE. In the case of PHOENIX, there is an option to use line profiles calculated in non-LTE for some species (Li I, Na I, K I, Ca I, Ca II). However, this option was only used for models with $T_{\rm eff} \geq 4000$ K, according to Husser et al. (2013).

One of the differences between the MARCS and PHOENIX models is in the abundances of elements assumed in the model calculations. In the case of MARCS, the reference solar abundance mixture is that of Grevesse et al. (2007). Furthermore, the variation of abundances as a function of metallicity used in the model grid examined here reflects the typical elemental abundance ratios in stars in the solar neighbourhood. Specifically, [α/Fe] increases from 0.0 at solar metallicity to +0.1 at [M/H] = −0.25 and +0.2 at [M/H] = −0.5, and further to +0.3 at [M/H] = −0.75 and +0.4 at [M/H] = −1.0. In the PHOENIX models, the reference solar abundances are taken from Asplund et al. (2009) in P2018, complemented by results from Caffau et al. (2011) in P2019. PHOENIX models with a range of [α/Fe] values are available for metallicities equal to or less than 0.0, but only for $T_{\rm eff} \geq 3500$ K. P2018 and P2019 used models with [α/Fe] = 0 exclusively in their analysis (see Sect. 3 in P2018).

The MARCS models used for the comparison are those included in the SME package, which were used in L2016 and L2017. The model data provided are the mass column density in units of g cm^{-2}, the temperature in units of K, the electron number density and the atomic number density in units of cm^{-3}, the density in units of g cm^{-3}, and the optical depth at a reference wavelength of 5000 Å.

The PHOENIX models used for the comparison were downloaded from the Göttingen Spectral Library[6] described in Husser et al. (2013). The online documentation states that for each atmospheric model the optical depth, the temperature in units of K, the gas pressure in units of dyn cm^{-2}, the density in units of g cm^{-3}, and the electron partial pressure in units of dyn cm^{-2} are provided. However, the downloaded data files do not contain the electron pressure. The optical depth in the PHOENIX data files is given at a reference wavelength of 12 000 Å, according to Husser et al. (2013). Thus, there are three quantities in common that can be compared: temperature, gas pressure, and density.

Figure 11 shows the gas pressure profiles of MARCS and PHOENIX model atmospheres as a function of temperature for four different effective temperatures and three different metallicities. The surface gravity is 4.5 dex in all cases. In the lower part of the atmosphere, the gas pressure is higher in PHOENIX models than in MARCS models at the same temperature, and the differences increase towards larger depths. The opposite is the case in the upper part of the atmosphere. The difference in density profiles shows a very similar behaviour. The differences increase towards smaller $T_{\rm eff}$ values, with maximum differences of about 0.3 dex (corresponding to a factor of two). Using $\log g = 5.0$ instead of $\log g = 4.5$ results in slightly smaller differences. The differences in gas pressure at the location where the temperature is equal to the effective temperature, corresponding to the

[4] Astrophysical Chemical Equilibrium Solver.
[5] Stoichiometric Equilibrium Solver for Atoms and Molecules.
[6] http://phoenix.astro.physik.uni-goettingen.de/?page_id=108, accessed June 2020.

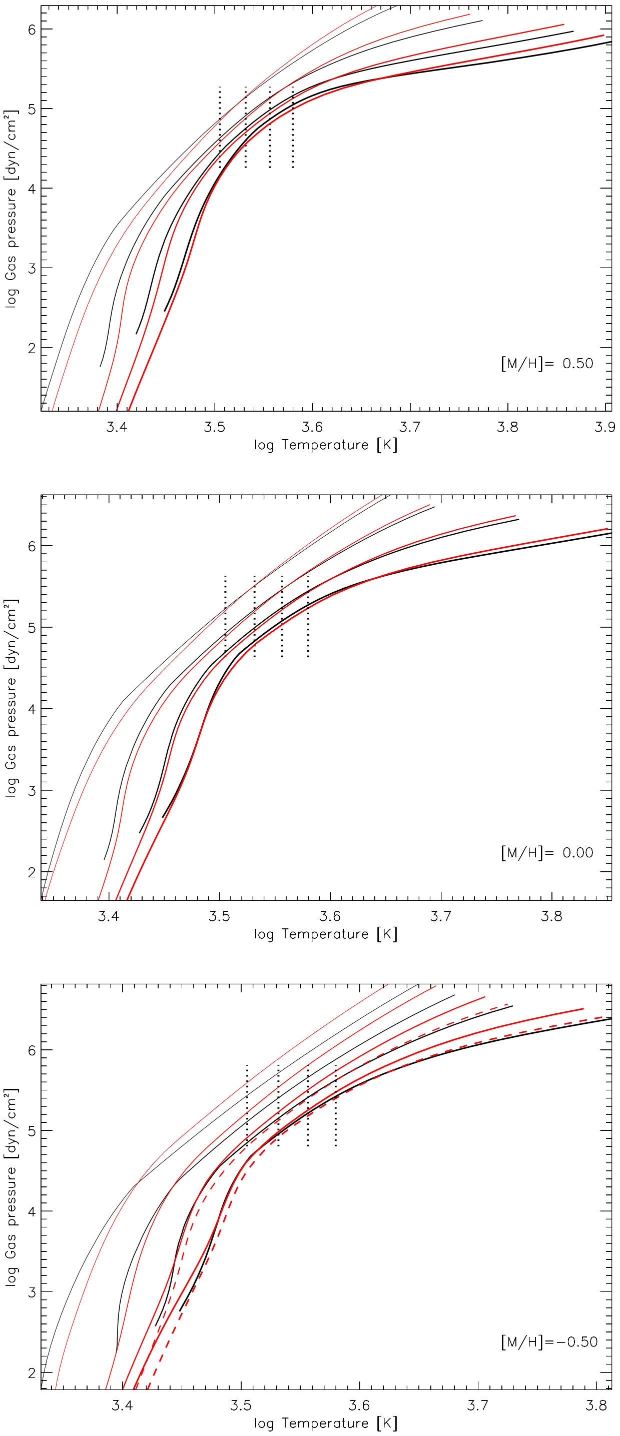

Fig. 11. Comparison of temperature–pressure profiles for `MARCS` (black solid lines) and `PHOENIX` (red solid lines) model atmospheres used by L2016 and L2017, and P2018 and P2019, respectively (see text for details). Each panel shows profiles for $T_{\rm eff}$ = 3200, 3400, 3600, and 3800 K (*from left to right*). Vertical dotted lines corresponding to the values of the effective temperatures are also shown. *Three panels*: profiles for three different metallicities (decreasing from the *top to the bottom panel*). The red dashed lines in the *bottom panel* correspond to `PHOENIX` models with [α/Fe] = +0.2 (for $T_{\rm eff}$ = 3600 and 3800 K).

line-forming region, are small, and range from being insignificant at $T_{\rm eff}$ = 3200 K to about 15% at $T_{\rm eff}$ = 3800 K (0.06 dex).

The differences are smallest at solar metallicity. They are slightly larger at [M/H] = +0.5 and even larger at [M/H] = −0.5, in particular in the lower part of the atmosphere, including the line-forming region. However, most of the difference at [M/H] = −0.5 seems to be due to the different abundances of α-elements used in the models. As mentioned above, `PHOENIX` models with [α/Fe] = +0.2 are available for $T_{\rm eff} \geq$ 3500 K. As can be seen in Fig. 11 (bottom panel) the profiles for these models closely follow those of the corresponding `MARCS` models, except in some parts of the upper atmosphere, above the line-forming region.

5. Conclusions

In recent years, many studies deriving M-dwarf atmospheric parameters have been published. We compared parameters derived from high-resolution optical and near-infrared spectra by L2016, L2017, P2018, P2019, and R2018 with each other for an overlapping sample of stars. In the case of effective temperature we also compared with effective temperatures derived from interferometric diameters and bolometric fluxes. We find that the effective temperatures generally agree, although the temperatures from P2018 and P2019 are often higher than those from L2016, L2017, and Rabus et al. (2019). R2018 agrees with L2016, L2017, P2018, and P2019 but shows a larger spread compared to Rabus et al. (2019). For the surface gravity we see a larger spread. The P2018 surface gravities are higher than those from L2016 and L2017 while the ones from P2019 are lower. R2018 surface gravities are higher than all other studies in most cases. The metallicity also shows a spread, where P2018 and P2019 metallicities are grouped around solar metallcities. Furthermore, the metallicities from P2019 obtained in the near-infrared are higher than the others. Metallicities from R2018 are spread over the whole parameter space and show no correlation with those provided by L2016, L2017, P2018, or P2019. The large discrepancy between the parameter values derived by R2018 and those from other studies can be explained by degeneracies between the metallicity and surface gravity. We identified some outliers, for example the star GJ 908 for which the effective temperature and surface gravity from L2017 and P2019 agree within uncertainties while the metallicities differ significantly. R2018 derived a metallicity 1 dex higher than what was derived by L2017 for this star.

We investigated the contribution of non-LTE effects to the difference in derived parameters. We generated synthetic spectra in LTE and non-LTE using grids of departure coefficients for Fe I and K I for the non-LTE spectra and compared these to each other. For iron we found the difference between LTE and non-LTE to be insignificant. For potassium the difference was larger. The largest difference was observed for lines with the lowest excitation energies. We quantified the effect by determining abundance corrections for K I lines in the near-infrared that were most affected (with the addition of the resonance line at 7699 Å). The largest abundance corrections of around −0.2 dex were found for the low-excitation lines in the warmest stars. Spectroscopically derived stellar parameters such as effective temperature and metallicity are also affected by non-LTE effects. We found that LTE underestimates $T_{\rm eff}$ while it overestimates the metallicity. The largest difference in $T_{\rm eff}$ was found for one of the warmest stars in the sample, GJ 880, which shows a difference of 213 K. The coolest star with the highest overall metallicity (GJ 179) shows the largest difference in metallicity, −0.24 dex.

This difference in metallicity between LTE and non-LTE could possibly partly explain why the metallicities derived in the near-infrared by P2019 are higher than the metallicities derived in the visual. The difficulties with fitting K I lines in the near-infrared reported by P2019 could also be explained by non-LTE effects[7].

We generated synthetic spectra with the parameters from L2016, L2017, P2018, and P2019 for four of the stars in the sample and assessed how well these reproduced observed near-infrared spectra through a χ^2 analysis. R2018 was excluded due to the possible degeneracy between the parameters. For all of the parameters, we found large differences for the strongest lines of potassium. Strong lines for other elements in general show a better fit. However, two of the stars that were identified as outliers when comparing the metallicity between L2016 and L2017 and P2018 and P2019 (GJ 179 and GJ 908) show high χ^2-values for non-potassium lines. This indicates a problem with the models and/or the derived parameters. Synthetic spectra generated using non-LTE for K I improved the χ^2-values for most of the potassium lines, except for the star GJ 176. An explanation for the K lines that are worse with P2019 parameters in non-LTE in all stars (except GJ 203) could be that the parameters were derived using LTE. This means that the best-fit parameters compensate for the non-LTE effects to some degree. When these parameters are then used in non-LTE they show a worse fit. However, this cannot explain the difference seen for the lines generated with parameters from L2016 and L2017, because K lines were excluded in that study. Another possible explanation is related to non-solar chemical abundances. In particular, for GJ 176 the potassium abundance in the atmosphere could be smaller than the solar abundance that was assumed in our analysis. This would weaken the K lines and hence give a better fit for lines generated in LTE. As can be seen in Fig. 4 the lines are weaker in the LTE spectra than in the non-LTE spectra.

The atmospheric models used by P2018, P2019, L2016, and L2017 agree fairly well, with most of the differences occurring near the surface or deep in the interior. The largest contribution to the differences in the results of the spectroscopic analyses is probably found for metal-poor stars because of the differences in the assumed [α/Fe] abundances. We also find that the difference in atmospheric models in the line-forming region increases towards higher effective temperatures. As the non-LTE effects of K also increase towards higher temperatures it is possible that these effects amplify each other. These effects could explain why the star GJ 908, which was identified as an outlier in Sect. 2.2, shows a large difference in metallicity. This star has a low metallicity and a rather high effective temperature. On the other hand, the star GJ 203 has a high surface gravity, corresponding to small model differences, and a fairly low effective temperature, and for this star the parameters of L2017 and P2018 and P2019 agree.

Another star that was given as an outlier in Sect. 2.2 was GJ 179 which has a low effective temperature indicating a small model difference and a high metallicity which indicates a slightly larger model difference. If we look at the leftmost curves in the top panel of Fig. 11 we see that the differences between `MARCS` and `PHOENIX` models are very small. Neither non-LTE effects nor model differences can fully explain the difference in derived metallicities for this star. We also see that this star has high χ^2-values for many lines, not only potassium lines (see Fig. 8). A possible explanation could again be non-solar abundances. High-resolution spectroscopic observations of this star covering a large wavelength range are needed to derive abundances of individual elements. GJ 849 was also identified as an outlier in Sect. 2.2. This star has similar effective temperature and metallicity to GJ 179 when looking at the parameters derived by L2016 and L2017 and could therefore be affected by non-LTE in the same way. However, L2016 derived a significantly lower effective temperature than P2018 and P2019, regardless of wavelength range.

Another major source of uncertainty for the derived parameters is the quality of the atomic data in the line list. We did not compare the atomic data used by L2016, L2017, P2018, P2019, and R2018 because the line lists from P2018 and P2019 are not available. However, a careful assessment of the available atomic data in the near-infrared should be done and the most precise and accurate data should be selected for any future analysis of high-resolution spectra. In addition, the magnetic sensitivity of the lines should be taken into account in order to assess the influence of magnetic fields on the derived parameters.

In conclusion, the cores of the strongest K I lines in the near-infrared are clearly affected by non-LTE and this needs to be taken into account in any analysis of high-resolution M-dwarf spectra in order to derive the most realistic parameters. We recommend that non-LTE be used for the calculation of model spectra or that the lines be avoided. Fe I can be calculated in LTE because the difference between LTE and non-LTE is insignificant. The effects of using non-LTE to derive the abundances of other elements remain to be investigated for M dwarfs. For example, some Ca I lines show a discrepancy between synthetic and observed spectra for some of the stars investigated here (see Fig. 6). The discrepancies could be due to inadequate data, but also non-LTE effects could provide a possible explanation because Ca I shows non-LTE effects in FGK stars (Mashonkina et al. 2017; Osorio et al. 2020).

In order to validate stellar parameters derived using spectroscopic methods, we need model-independent stellar parameters to compare with, such as $T_{\rm eff}$ from interferometry. Further research into asteroseismology for M dwarfs is also needed so that $\log g$ can be constrained without using empirical calibrations. With a well-defined set of fully characterised M-dwarf benchmark stars we will be able to disentangle the contribution of non-LTE effects to uncertainties in the spectroscopic analysis from other possible contributors, such as the atmospheric model structure, atomic data, and non-solar abundances of individual elements.

Acknowledgements. We thank Anish Amarsi for providing the non-LTE grid for potassium and for fruitful discussions. We acknowledge support from the Swedish National Space Agency (SNSA/Rymdstyrelsen) and the Swedish Research Council (Vetenskapsrådet). This work has made use of the VALD database, operated at Uppsala University, the Institute of Astronomy RAS in Moscow, and the University of Vienna.

References

Allard, F., Homeier, D., Freytag, B., et al. 2013, Mem. Soc. Astron. It. Suppl., 24, 128
Amarsi, A. M., Lind, K., Asplund, M., Barklem, P. S., & Collet, R. 2016, MNRAS, 463, 1518
Amarsi, A. M., Lind, K., Osorio, Y., et al. 2020, A&A, 642, A62
Asplund, M. 2005, ARA&A, 43, 481
Asplund, M., Grevesse, N., Sauval, A. J., & Scott, P. 2009, ARA&A, 47, 481
Baraffe, I., Chabrier, G., Allard, F., & Hauschildt, P. H. 1998, A&A, 337, 403
Barklem, P. S., Piskunov, N., & O'Mara, B. J. 2000, A&AS, 142, 467
Bean, J. L., Benedict, G. F., & Endl, M. 2006, ApJ, 653, L65
Benedict, G. F., Henry, T. J., Franz, O. G., et al. 2016, AJ, 152, 141
Birky, J., Hogg, D. W., Mann, A. W., & Burgasser, A. 2020, ApJ, 892, 31
Blackwell-Whitehead, R., Pavlenko, Y. V., Nave, G., et al. 2011, A&A, 525, A44
Boyajian, T. S., von Braun, K., van Belle, G., et al. 2012, ApJ, 757, 112
Bressan, A., Marigo, P., Girardi, L., et al. 2012, MNRAS, 427, 127
Browning, M. K. 2008, ApJ, 676, 1262

[7] P2018 and P2019 removed K lines which showed a poor fit (V. Passegger, priv. comm.). This would mitigate some of the biases in stellar parameters arising from not accounting for non-LTE effects in potassium.

Caffau, E., Ludwig, H. G., Steffen, M., Freytag, B., & Bonifacio, P. 2011, Sol. Phys., 268, 255
Chen, Y., Girardi, L., Bressan, A., et al. 2014, MNRAS, 444, 2525
Davis, S. P., Phillips, J. G., & Littleton, J. E. 1986, ApJ, 309, 449
Donati, J. F., Kouach, D., Moutou, C., et al. 2020, MNRAS, 498, 5684
Dorn, R. J., Follert, R., Bristow, P., et al. 2016, SPIE Conf. Ser., 9908, 99080I
Dorn, C., Venturini, J., Khan, A., et al. 2017, A&A, 597, A37
Dressing, C. D., & Charbonneau, D. 2015, ApJ, 807, 45
Gaia Collaboration (Prusti, T., et al.) 2016, A&A, 595, A1
Gaia Collaboration (Brown, A. G. A., et al.) 2018, A&A, 616, A1
Gilmore, G., Randich, S., Asplund, M., et al. 2012, The Messenger, 147, 25
Goldman, A., Schoenfeld, W. G., Goorvitch, D., et al. 1998, J. Quant. Spectr. Rad. Transf., 59, 453
Gray, R. O., & Corbally, Christopher, J. 2009, Stellar Spectral Classification (Princeton: Princeton University Press)
Grevesse, N., & Sauval, A. J. 1998, Space Sci. Rev., 85, 161
Grevesse, N., Asplund, M., & Sauval, A. J. 2007, Space Sci. Rev., 130, 105
Gustafsson, B., Edvardsson, B., Eriksson, K., et al. 2008, A&A, 486, 951
Henry, T. J., Jao, W.-C., Subasavage, J. P., et al. 2006, AJ, 132, 2360
Husser, T. O., Wende-von Berg, S., Dreizler, S., et al. 2013, A&A, 553, A6
Jeffers, S. V., Schöfer, P., Lamert, A., et al. 2018, A&A, 614, A76
Korotin, S. A., Andrievsky, S. M., Caffau, E., Bonifacio, P., & Oliva, E. 2020, MNRAS, 496, 2462
Kurucz, R. L. 1995, Robert L. Kurucz on-line database of molecular line lists, MgH A-X and B'-X transitions, (KMGH), http://kurucz.harvard.edu/linelists/linesmol/mgh.asc
Kurucz, R. L. 2007, Robert L. Kurucz on-line database of observed and predicted atomic transitions, http://kurucz.harvard.edu/atoms/2000/
Kurucz, R. L. 2008, Robert L. Kurucz on-line database of observed and predicted atomic transitions, http://kurucz.harvard.edu/atoms/2800/
Kurucz, R. L. 2009, Robert L. Kurucz on-line database of observed and predicted atomic transitions, http://kurucz.harvard.edu/atoms/2100/, 2300/
Kurucz, R. L. 2010, Robert L. Kurucz on-line database of observed and predicted atomic transitions, http://kurucz.harvard.edu/atoms/2200/, 2400/
Kurucz, R. L. 2012, Robert L. Kurucz on-line database of observed and predicted atomic transitions, http://kurucz.harvard.edu/atoms/1501/, 1900/
Kurucz, R. L. 2014, Robert L. Kurucz on-line database of observed and predicted atomic transitions, http://kurucz.harvard.edu/atoms/2600/
Kurucz, R. L., & Peytremann, E. 1975, SAO Sp. Rep., 362, 1
Kuznetsov, M. K., del Burgo, C., Pavlenko, Y. V., & Frith, J. 2019, ApJ, 878, 134
Lawler, J. E., Guzman, A., Wood, M. P., Sneden, C., & Cowan, J. J. 2013, ApJS, 205, 11
Lind, K., Bergemann, M., & Asplund, M. 2012, MNRAS, 427, 50
Lindgren, S., & Heiter, U. 2017, A&A, 604, A97
Lindgren, S., Heiter, U., & Seifahrt, A. 2016, A&A, 586, A100
López-Valdivia, R., Mace, G. N., Sokal, K. R., et al. 2019, ApJ, 879, 105
Mann, A. W., Feiden, G. A., Gaidos, E., Boyajian, T., & von Braun, K. 2015, ApJ, 804, 64
Martin, G., Fuhr, J., & Wiese, W. 1988, J. Phys. Chem. Ref. Data Suppl., 17, 1
Mashonkina, L., Sitnova, T., & Belyaev, A. K. 2017, A&A, 605, A53
Mayor, M., Pepe, F., Queloz, D., et al. 2003, The Messenger, 114, 20
Meyer, M. 2017, PhD thesis, Universität Hamburg, Germany
Neves, V., Bonfils, X., Santos, N. C., et al. 2014, A&A, 568, A121
O'Brian, T. R., Wickliffe, M. E., Lawler, J. E., Whaling, W., & Brault, J. W. 1991, J. Opt. Soc. Am. B Opt. Phys., 8, 1185
Osorio, Y., Allende Prieto, C., Hubeny, I., Mészáros, S., & Shetrone, M. 2020, A&A, 637, A80
Pancino, E., Lardo, C., Altavilla, G., et al. 2017, A&A, 598, A5
Passegger, V. M., Wende-von Berg, S., & Reiners, A. 2016, A&A, 587, A19
Passegger, V. M., Reiners, A., Jeffers, S. V., et al. 2018, A&A, 615, A6
Passegger, V. M., Schweitzer, A., Shulyak, D., et al. 2019, A&A, 627, A161
Penkin, N. P., & Komarovskii, V. A. 1976, J. Quant. Spectr. Rad. Transf., 16, 217
Piskunov, N., & Valenti, J. A. 2017, A&A, 597, A16
Piskunov, N. E., Kupka, F., Ryabchikova, T. A., Weiss, W. W., & Jeffery, C. S. 1995, A&AS, 112, 525
Quirrenbach, A., Amado, P. J., Mandel, H., et al. 2010, SPIE Conf. Ser., 7735, 773513
Rabus, M., Lachaume, R., Jordán, A., et al. 2019, MNRAS, 484, 2674
Rajpurohit, A. S., Allard, F., Rajpurohit, S., et al. 2018, A&A, 620, A180
Ralchenko, Y., Kramida, A., Reader, J., & NIST ASD Team 2010, NIST Atomic Spectra Database (ver. 4.0.0)
Randich, S., Gilmore, G., & Gaia-ESO Consortium. 2013, The Messenger, 154, 47
Rauer, H., Catala, C., Aerts, C., et al. 2014, Exp. Astron., 38, 249
Reggiani, H., Amarsi, A. M., Lind, K., et al. 2019, A&A, 627, A177
Reiners, A. 2012, Liv. Rev. Sol. Phys., 9, 1
Reiners, A., Zechmeister, M., Caballero, J. A., et al. 2018, A&A, 612, A49
Ricker, G. R., Winn, J. N., Vanderspek, R., et al. 2015, J. Astron. Teles. Instrum. Syst., 1, 014003
Rodríguez-López, C. 2019, Front. Astron. Space Sci., 6, 76
Rojas-Ayala, B., Covey, K. R., Muirhead, P. S., & Lloyd, J. P. 2012, ApJ, 748, 93
Ryabchikova, T., Piskunov, N., Kurucz, R. L., et al. 2015, Phys. Scr, 90, 054005
Smith, W., & Missen, R. 1982, Chemical Reaction Equilibrium Analysis (Hoboken: Wiley)
Souto, D., Cunha, K., Smith, V. V., et al. 2020, ApJ, 890, 133
Thiabaud, A., Marboeuf, U., Alibert, Y., Leya, I., & Mezger, K. 2015, A&A, 580, A30
Valenti, J. A., & Piskunov, N. 1996, A&AS, 118, 595
Veyette, M. J., Muirhead, P. S., Mann, A. W., et al. 2017, ApJ, 851, 26
Ward, L., Vogel, O., Arnesen, A., Hallin, R., & Wännström, A. 1985, Phys. Scr., 31, 161
Wenger, M., Ochsenbein, F., Egret, D., et al. 2000, A&AS, 143, 9
Wiese, W. L., Smith, M. W., & Miles, B. M. 1969, Atomic Transition Probabilities: Sodium through Calcium. A Critical Data Compilation, eds. W. L. Wiese, M. W. Smith, & B. M. Miles (USA: US Government Printing Office), 2
Yadav, R. K., Christensen, U. R., Morin, J., et al. 2015, ApJ, 813, L31

Appendix A: Derived parameters

This appendix provides a table with the stellar atmospheric parameters derived by L2016, L2017, P2018, P2019, and R2018 referred to in Sect. 2.2.

Table A.1. Atmospheric stellar parameters from Lindgren et al. (2016), Lindgren & Heiter (2017), Passegger et al. (2018, 2019), and Rajpurohit et al. (2018) (references L2016, L2017, P2018, P2019, and R2018 in column "Ref.", respectively) for the stars in the sample.

Star	Ref.	$T_{\rm eff}$ [K]	$\log\ g$ [cm s^{-2}]	[M/H]	$v \sin i$ [km s^{-1}]	$v_{\rm mic}$ [km s^{-1}]	$v_{\rm mac}$ [km s^{-1}]
1 GJ176	P2018V	3582 ± 51	4.88 ± 0.07	−0.08 ± 0.16	3.00	0.25	0.50
	P2019V	3520 ± 51	4.79 ± 0.04	−0.08 ± 0.16	2.00	0.25	0.50
	P2019N	3654 ± 56	4.66 ± 0.04	+0.48 ± 0.16	2.00	0.25	0.50
	P2019NV	3689 ± 54	4.66 ± 0.06	+0.33 ± 0.19	2.00	0.25	0.50
	R2018NV	3500 ± 100	5.10 ± 0.30	0.00 ± 0.30	...	...	...
	L2016	3550 ± 100	4.76 ± 0.08	+0.11 ± 0.09	1.00	1.00	2.01
2 GJ179	P2018V	3391 ± 51	5.00 ± 0.07	0.00 ± 0.16	2.50	0.20	0.40
	P2019V	3339 ± 51	4.85 ± 0.04	+0.02 ± 0.16	2.00	0.20	0.40
	P2019N	3349 ± 56	4.80 ± 0.04	+0.14 ± 0.16	2.00	0.20	0.40
	P2019NV	3341 ± 54	4.84 ± 0.06	+0.04 ± 0.19	2.00	0.20	0.40
	R2018NV	3300 ± 100	5.00 ± 0.30	+0.30 ± 0.30	...	...	...
	L2017	3300 ± 100	4.89 ± 0.10	+0.36 ± 0.04	1.00	0.25	0.06
3 GJ203	P2018V	3362 ± 51	5.03 ± 0.07	−0.03 ± 0.16	3.00	0.25	0.50
	P2019V	3332 ± 51	4.86 ± 0.04	−0.01 ± 0.16	2.00	0.25	0.50
	P2019N	3379 ± 56	4.83 ± 0.04	0.00 ± 0.16	2.00	0.25	0.50
	P2019NV	3335 ± 54	4.85 ± 0.06	0.00 ± 0.19	2.00	0.25	0.50
	R2018NV	3400 ± 100	5.10 ± 0.30	+0.40 ± 0.30	...	...	...
	L2017	3425 ± 100	5.01 ± 0.10	−0.13 ± 0.04	1.00	0.25	0.02
4 GJ436	P2018V	3512 ± 51	4.90 ± 0.07	−0.02 ± 0.16	3.00	0.25	0.50
	P2019V	3459 ± 51	4.79 ± 0.04	−0.01 ± 0.16	2.00	0.25	0.50
	P2019N	3571 ± 56	4.69 ± 0.04	+0.30 ± 0.16	2.00	0.25	0.50
	P2019NV	3472 ± 54	4.77 ± 0.06	+0.03 ± 0.19	2.00	0.25	0.50
	R2018NV	3500 ± 100	4.00 ± 0.30	−0.50 ± 0.30	...	...	...
	L2016	3400 ± 100	4.80 ± 0.08	+0.03 ± 0.06	1.00	1.00	0.08
5 GJ514	P2018V	3704 ± 51	4.82 ± 0.07	−0.15 ± 0.16	3.00	0.30	0.60
	P2019V	3720 ± 51	4.69 ± 0.04	+0.07 ± 0.16	2.00	0.30	0.60
	P2019N	3722 ± 56	4.67 ± 0.04	+0.18 ± 0.16	2.00	0.30	0.60
	P2019NV	3745 ± 54	4.67 ± 0.06	+0.14 ± 0.19	2.00	0.30	0.60
	R2018NV	3700 ± 100	5.20 ± 0.30	−0.40 ± 0.30	...	...	...
	L2017	3727 ± 100	4.78 ± 0.10	+0.07 ± 0.07	1.30	0.35	0.27
6 GJ581	P2018V	3430 ± 51	5.00 ± 0.07	−0.09 ± 0.16	3.00	0.25	0.50
	P2019V	3415 ± 51	4.85 ± 0.04	−0.02 ± 0.16	2.00	0.25	0.50
	P2019N	3424 ± 56	4.83 ± 0.04	+0.03 ± 0.16	2.00	0.25	0.50
	P2019NV	3413 ± 54	4.85 ± 0.06	−0.02 ± 0.19	2.00	0.25	0.50
	R2018NV	3400 ± 100	5.00 ± 0.30	0.00 ± 0.30	...	...	...
	L2016	3350 ± 100	4.92 ± 0.08	−0.02 ± 0.13	1.00	1.00	0.33
7 GJ628	P2018V	3378 ± 51	5.01 ± 0.07	+0.01 ± 0.16	3.00	0.20	0.40
	P2019V	3320 ± 51	4.75 ± 0.04	−0.01 ± 0.16	2.00	0.20	0.40
	P2019N	3353 ± 56	4.73 ± 0.04	+0.07 ± 0.16	2.00	0.20	0.40
	P2019NV	3305 ± 54	4.75 ± 0.06	+0.01 ± 0.19	2.00	0.20	0.40
	R2018NV	3400 ± 100	5.00 ± 0.30	+0.40 ± 0.30	...	...	...
	L2016	3275 ± 100	4.93 ± 0.08	+0.12 ± 0.14	1.00	1.00	0.04
8 GJ849	P2018V	3454 ± 51	4.96 ± 0.07	−0.01 ± 0.16	3.00	0.25	0.50
	P2019V	3414 ± 51	4.82 ± 0.04	+0.05 ± 0.16	2.00	0.25	0.50
	P2019N	3633 ± 56	4.68 ± 0.04	+0.54 ± 0.16	2.00	0.25	0.50
	P2019NV	3427 ± 54	4.80 ± 0.06	+0.09 ± 0.19	2.00	0.25	0.50
	R2018NV	3400 ± 100	5.10 ± 0.30	+0.30 ± 0.30	...	...	...
	L2016	3350 ± 100	4.76 ± 0.08	+0.28 ± 0.07	1.00	1.00	0.05

Notes. The letters V, N, and NV in column "Ref." indicate the wavelength regions (visual, near-infrared, and both combined) which P2018, P2019, and R2018 used to derive the parameters. R2018 has no specified $v \sin i$, $v_{\rm mic}$, nor $v_{\rm mac}$.

Table A.1. continued.

Star	Ref.	$T_{\rm eff}$ [K]	log g [cm s^{-2}]	[M/H]	$v \sin i$ [km s^{-1}]	$v_{\rm mic}$ [km s^{-1}]	$v_{\rm mac}$ [km s^{-1}]
	P2018V	3359 ± 51	5.01 ± 0.07	+0.06 ± 0.16	2.50	0.20	0.40
	P2019V	3317 ± 51	4.75 ± 0.04	0.00 ± 0.16	2.00	0.20	0.40
9 GJ876	P2019N	3286 ± 56	4.74 ± 0.04	+0.05 ± 0.16	2.00	0.20	0.40
	P2019NV	3305 ± 54	4.75 ± 0.06	0.00 ± 0.19	2.00	0.20	0.40
	R2018NV	3200 ± 100	5.00 ± 0.30	+0.40 ± 0.30	...	...	...
	L2016	3250 ± 100	4.89 ± 0.08	+0.19 ± 0.15	1.00	1.00	0.05
	P2018V	3787 ± 51	4.70 ± 0.07	+0.10 ± 0.16	2.50	0.30	0.60
	P2019V	3789 ± 51	4.65 ± 0.04	+0.32 ± 0.16	2.00	0.30	0.60
10 GJ880	2P019N	3784 ± 56	4.65 ± 0.04	+0.53 ± 0.16	2.00	0.30	0.60
	P2019NV	3810 ± 54	4.65 ± 0.06	+0.38 ± 0.19	2.00	0.30	0.60
	R2018NV	3700 ± 100	5.50 ± 0.30	+0.30 ± 0.30	...	...	...
	L2017	3720 ± 100	4.74 ± 0.10	+0.20 ± 0.05	2.07	0.35	0.15
	P2018V	3657 ± 51	4.84 ± 0.07	−0.12 ± 0.16	3.00	0.30	0.60
	P2019V	3630 ± 51	4.73 ± 0.04	−0.01 ± 0.16	2.00	0.30	0.60
11 GJ908	P2019N	3651 ± 56	4.78 ± 0.04	−0.22 ± 0.16	2.00	0.30	0.60
	P2019NV	3626 ± 54	4.73 ± 0.06	−0.02 ± 0.19	2.00	0.30	0.60
	R2018NV	3600 ± 100	5.50 ± 0.30	+0.50 ± 0.30	...	...	...
	L2017	3646 ± 100	4.86 ± 0.10	−0.51 ± 0.05	2.25	0.35	3.70

Appendix B: Atomic and molecular data

This appendix provides two tables with the atomic and molecular data in the optical and near-infrared wavelength regions, referred to in Sect. 3.1.

Table B.1. Atomic and molecular data for selected lines with an estimated central depth larger than 0.01 in a wavelength region around the K I resonance line at 7699 Å.

Species	λ [Å]	E_{low} [eV]	$\log gf$	$\log \gamma_{\text{rad}}$	$\log \gamma_{\text{Waals}}$	References
TiO	7697.0118	0.3741	0.041	7.020	0.000	
TiO	7697.0118	0.4150	−0.238	6.997	0.000	
TiO	7697.0178	0.3141	−0.580	7.029	0.000	
TiO	7697.0415	0.1539	−0.723	7.016	0.000	
TiO	7697.2015	0.2153	−0.108	7.007	0.000	
TiO	7697.2074	0.6242	−0.043	6.964	0.000	
TiO	7697.5630	0.7979	0.036	6.949	0.000	
TiO	7697.5630	0.2903	−0.360	7.006	0.000	
Sc	7697.7703	2.5689	−0.410	8.190	−7.710	K09
TiO	7698.1972	0.5280	−0.018	7.003	0.000	
TiO	7698.2091	0.4021	−0.147	6.985	0.000	
TiO	7698.2447	0.2202	−0.097	7.007	0.000	
TiO	7698.2921	0.3794	0.052	7.020	0.000	
TiO	7698.2921	0.1568	−0.699	7.016	0.000	
TiO	7698.4936	0.3176	−0.558	7.028	0.000	
TiO	7698.6656	0.4169	0.115	6.990	0.000	
K	7698.9643	0.0000	−0.154	7.600	−7.445	K12, BPM
TiO	7699.3000	0.2253	−0.086	7.006	0.000	
TiO	7699.3178	0.6354	−0.038	6.963	0.000	
OH	7699.4606	0.0952	−8.073	0.000	0.000	GSGCD
TiO	7699.4838	0.4107	−0.141	6.984	0.000	
TiO	7699.4838	0.1598	−0.678	7.015	0.000	
Yb	7699.4870	2.4438	−0.034	0.000	0.000	PK
TiO	7699.6320	0.5754	0.215	6.977	0.000	
TiO	7699.6498	0.5362	−0.012	7.002	0.000	
TiO	7699.6498	0.3848	0.062	7.019	0.000	
TiO	7699.6498	0.2967	−0.351	7.005	0.000	
TiO	7699.6617	0.4234	−0.230	6.996	0.000	
OH	7699.9474	0.0954	−8.073	0.000	0.000	GSGCD
TiO	7699.9760	0.3211	−0.537	7.027	0.000	
TiO	7700.3081	0.8108	0.040	6.947	0.000	
Ti	7700.3312	3.1608	−1.757	7.260	−7.770	K10
TiO	7700.3852	0.2305	−0.075	7.006	0.000	
Ti	7700.6473	3.1608	−1.914	7.260	−7.770	K10
TiO	7700.6996	0.4255	0.122	6.989	0.000	
TiO	7700.6996	0.1629	−0.657	7.015	0.000	
TiO	7700.7886	0.4193	−0.135	6.983	0.000	
MgH	7700.8709	1.2288	−1.377	7.060	0.000	KMGH
MgH	7700.8709	1.2288	−1.632	7.060	0.000	KMGH

Notes. All lines are from neutral species. λ … wavelength, E_{low} … lower level energy, $\log gf$ … logarithm (base 10) of the product of the oscillator strength of the transition and the statistical weight of the lower level, $\log \gamma_{\text{rad}}$ … logarithm of the radiative damping width in units of rad s^{-1}, $\log \gamma_{\text{Waals}}$ … logarithm of the van der Waals broadening width per unit perturber number density at 10 000 K in units of rad s^{-1} cm^3. Unknown damping parameters are set to zero.

References. For TiO lines: Davis et al. (1986). References for other lines: BPM … Barklem et al. (2000), GSGCD … Goldman et al. (1998), K09 … Kurucz (2009), K10 … Kurucz (2010), KMGH … Kurucz (1995), PK … Penkin & Komarovskii (1976), K12 … Kurucz (2012).

Table B.2. Atomic data for selected lines with an estimated central depth larger than 0.15 in wavelength regions around the near-infrared lines investigated in Sects. 3 and 4.

Species	λ [Å]	$E_{\rm low}$ [eV]	$\log gf$	$\log \gamma_{\rm rad}$	$\log \gamma_{\rm Waals}$	References
Cr	11015.530	3.4493	−0.429	8.370	−7.530	K10
K	11019.848	2.6700	−0.010	7.540	−6.661	WSM, BPM
K	11022.653	2.6702	−0.161	7.560	−6.661	K12, BPM
Cr	11044.610	3.0111	−1.930	6.980	−7.780	K10
OH	11066.781	0.7819	−5.947	0.000	0.000	GSGCD
OH	11066.781	0.7819	−5.947	0.000	0.000	GSGCD
OH	11068.946	0.7826	−5.948	0.000	0.000	GSGCD
OH	11068.946	0.7826	−5.948	0.000	0.000	GSGCD
Fe	11607.572	2.1979	−2.009	7.160	−7.820	BWL
Cr	11610.560	3.3212	0.055	7.850	−7.640	K10
Fe	11638.260	2.1759	−2.214	7.170	−7.820	BWL
Fe	11689.972	2.2227	−2.068	7.150	−7.820	BWL
K	11690.220	1.6100	0.250	7.810	−7.326	WSM, BPM
Ca	11759.570	4.5313	−0.878	7.500	−7.090	K07
Ca	11767.481	4.5322	−0.536	7.500	−7.090	K07
Ca	11769.345	4.5322	−1.011	7.500	−7.090	K07
K	11769.639	1.6171	−0.450	7.810	−7.326	WSM, BPM
K	11772.838	1.6171	0.510	7.810	−7.326	WSM, BPM
Ti	11780.542	1.4432	−2.170	6.870	−7.790	LGWSC
Fe	11783.265	2.8316	−1.574	6.750	−7.820	BWL
Ca	11793.043	4.5347	−0.258	7.500	−7.090	K07
Ca	11795.763	4.5347	−1.008	7.500	−7.090	K07
Ti	11797.186	1.4298	−2.280	6.900	−7.790	LGWSC
Mg	11828.171	4.3458	−0.333	0.000	−7.192	NIST10, BPM
Fe	11882.844	2.1979	−1.668	7.170	−7.820	BWL
Fe	11884.083	2.2227	−2.083	7.160	−7.820	BWL
Ti	11892.877	1.4298	−1.730	6.930	−7.790	LGWSC
V	11911.885	2.3654	−0.874	6.340	−7.780	K09
Ti	11949.547	1.4432	−1.570	6.900	−7.790	LGWSC
Ca	11955.955	4.1308	−0.849	8.010	−7.300	K07
Fe	11973.046	2.1759	−1.483	7.190	−7.820	BWL
Ti	11973.847	1.4601	−1.390	6.870	−7.790	LGWSC
Mg	12083.278	5.7532	0.450	0.000	0.000	KP
Mg	12083.649	5.7532	0.410	7.470	−6.981	NIST10
Ca	12105.841	4.5541	−0.305	7.420	−7.090	K07
Fe	12190.098	3.6352	−2.330	8.070	−7.750	BWL
Na	12311.480	3.7526	−1.007	0.000	0.000	NIST10
Na	12319.980	3.7533	−0.753	0.000	0.000	NIST10
K	12432.273	1.6100	−0.439	7.790	−7.022	WSM, BPM
Ca	12433.748	5.0261	−0.066	7.940	−7.090	K07
Ti	12484.617	1.5025	−3.277	6.870	−7.780	K10
Cr	12521.810	2.7079	−1.587	7.290	−7.800	K10
K	12522.134	1.6171	−0.139	7.790	−7.021	WSM, BPM
Cr	12532.840	2.7088	−1.879	7.290	−7.800	K10
Fe	12556.996	2.2786	−3.626	7.160	−7.820	BWL
Ti	12569.571	2.1747	−2.050	6.540	−7.810	LGWSC
Ti	12600.277	1.4432	−2.320	6.810	−7.790	LGWSC
Ca	12610.942	5.0486	−0.063	8.020	−6.770	K07
Fe	12638.703	4.5585	−0.783	8.440	−7.540	K14
Fe	12648.741	4.6070	−1.140	8.420	−7.540	BWL
Ti	12671.096	1.4298	−2.360	6.820	−7.790	LGWSC

Notes. All lines are from neutral species. For column descriptions see Table B.1.

References. B-WPNP . . . Blackwell-Whitehead et al. (2011), BPM . . . Barklem et al. (2000), BWL . . . O'Brian et al. (1991), GSGCD . . . Goldman et al. (1998), K07 . . . Kurucz (2007), K08 . . . Kurucz (2008), K09 . . . Kurucz (2009), K10 . . . Kurucz (2010), K12 . . . Kurucz (2012), K12 . . . Kurucz (2012), K14 . . . Kurucz (2014), KP . . . Kurucz & Peytremann (1975), LGWSC . . . Lawler et al. (2013), MFW . . . Martin et al. (1988), NIST10 . . . Ralchenko et al. (2010), NIST10 . . . Ralchenko et al. (2010), WSM . . . Wiese et al. (1969), WSM . . . Wiese et al. (1969), WV . . . Ward et al. (1985).

Table B.2. continued.

Species	λ [Å]	$E_{\rm low}$ [eV]	$\log gf$	$\log \gamma_{\rm rad}$	$\log \gamma_{\rm Waals}$	References
Na	12679.170	3.6170	−0.043	0.000	−6.653	NIST10, BPM
Na	12679.170	3.6170	−1.344	0.000	−6.653	NIST10, BPM
Na	12679.220	3.6170	−0.197	0.000	−6.653	NIST10, BPM
Ti	12738.383	2.1747	−1.280	7.950	−7.750	LGWSC
Ti	12744.905	2.4875	−1.280	7.530	−7.770	LGWSC
Fe	12807.152	3.6398	−2.452	8.080	−7.750	K14
Ti	12811.478	2.1603	−1.390	7.990	−7.750	LGWSC
Ca	12816.045	3.9104	−0.765	8.280	−7.520	K07
Ti	12821.672	1.4601	−1.190	6.810	−7.790	LGWSC
Ca	12823.867	3.9104	−0.997	8.280	−7.520	K07
Ca	12827.059	3.9104	−1.478	8.280	−7.520	K07
Ti	12831.445	1.4298	−1.490	6.820	−7.790	LGWSC
Ti	12847.034	1.4432	−1.330	6.820	−7.790	LGWSC
Fe	12879.766	2.2786	−3.458	7.170	−7.820	BWL
Ca	12885.290	4.4300	−1.164	7.770	−7.710	K07
Mn	12899.760	2.1142	−1.070	0.000	0.000	B-WPNP
V	12901.212	1.9553	−1.052	6.890	−7.780	K09
Ca	12909.070	4.4300	−0.224	7.770	−7.710	K07
Cr	12910.090	2.7079	−1.779	7.260	−7.800	K10
Ti	12919.899	2.1535	−1.560	8.000	−7.750	LGWSC
Cr	12921.810	2.7088	−2.743	7.260	−7.800	K10
Ni	12932.313	2.7403	−2.523	7.680	−7.810	K08
Cr	12937.020	2.7099	−1.896	7.260	−7.800	K10
Mn	12975.910	2.8884	−1.090	0.000	0.000	B-WPNP
Ti	12987.567	2.5057	−1.550	7.530	−7.770	LGWSC
Ca	13001.402	4.4410	−1.139	7.770	−7.710	K07
Ti	13005.365	2.1747	−2.287	7.990	−7.750	K10
Fe	13006.684	2.9904	−3.744	6.120	−7.810	K14
Ti	13011.250	2.1603	−2.180	8.000	−7.750	LGWSC
Ti	13011.897	1.4432	−2.270	6.820	−7.790	LGWSC
Ca	13033.554	4.4410	−0.064	7.770	−7.710	K07
Ca	13057.885	4.4410	−1.092	7.770	−7.710	K07
Ti	13077.265	1.4601	−2.220	6.820	−7.790	LGWSC
Ca	13086.430	4.4430	−1.214	7.810	−7.690	K07
V	13104.517	1.9496	−1.238	6.890	−7.780	K09
Al	13123.410	3.1427	0.270	0.000	0.000	WSM
Ca	13134.942	4.4506	0.085	7.770	−7.710	K07
Al	13150.753	3.1427	−0.030	0.000	0.000	WSM
Ca	13167.759	4.4506	−1.092	7.770	−7.710	K07
Cr	13201.150	2.7088	−1.834	7.250	−7.800	K10
Cr	13217.020	2.7099	−2.302	7.250	−7.800	K10
Ca	13250.322	4.5541	−1.033	7.560	−7.100	K07
Ti	13255.812	2.2312	−2.119	6.260	−7.810	K10
Mn	13281.490	2.9197	−1.350	0.000	0.000	B-WPNP
Fe	13287.829	2.9488	−3.021	6.130	−7.810	BWL
V	13291.120	1.9452	−1.570	0.000	0.000	MFW
V	13291.285	1.9452	−1.406	6.880	−7.780	K09
Mn	13293.800	2.1427	−1.580	0.000	0.000	B-WPNP
Ti	13305.697	2.2393	−1.863	6.080	−7.810	K10
Ca	13317.984	4.6244	−0.480	7.660	−7.130	K07
Mn	13318.940	2.1427	−1.370	0.000	0.000	B-WPNP
Ti	13346.704	2.2497	−2.243	5.820	−7.800	K10
Lu	13371.782	0.0000	−1.000	0.000	0.000	WV
Fe	13392.102	5.3516	−0.125	8.220	−7.480	K14
Mn	15159.158	4.8889	0.619	8.040	−7.520	K07
K	15163.067	2.6700	0.689	7.640	−7.320	K12
K	15163.067	2.6700	−0.613	7.640	−7.320	K12
K	15168.376	2.6702	0.480	7.620	0.000	WSM